RECONSTRUCTING PALEO-SMT POSITIONS ON THE CASCADIA MARGIN USING MAGNETIC SUSCEPTIBILITY
Final Scientific Report

October 1, 2012 – September 30, 2014

Joel E. Johnson and Stephen C. Phillips

Report issued May 2015

DOE Award No.: DE-FE0010120

University of New Hampshire
Department of Earth Sciences
56 College Rd. James Hall
Durham, NH 03824

DISCLAIMER

"This report was prepared as an account of work sponsored by an agency of the United States Government. Neither the United States Government nor any agency thereof, nor any of their employees, makes any warranty, express or implied, or assumes any legal liability or responsibility for the accuracy, completeness, or usefulness of any information, apparatus, product, or process disclosed, or represents that its use would not infringe privately owned rights. Reference herein to any specific commercial product, process, or service by trade name, trademark, manufacturer, or otherwise does not necessarily constitute or imply its endorsement, recommendation, or favoring by the United States Government or any agency thereof. The views and opinions of authors expressed herein do not necessarily state or reflect those of the United States Government or any agency thereof."

ABSTRACT

Magnetic susceptibility (κ) is a mixed signal in marine sediments, representing primary depositional and secondary diagenetic processes. Production of hydrogen sulfide via anaerobic oxidation of methane (AOM) at the sulfate-methane transition (SMT) and organoclastic sulfate reduction above the SMT can result in the dissolution of iron oxides, altering κ in sediments in methane gas and gas hydrate bearing regions. We investigated records of κ on the Cascadia margin (ODP Sites 1249 and 1252; IODP Site 1325) using a Zr/Rb heavy mineral proxy from XRF core scanning to identify intervals of primary detrital magnetic susceptibility and intervals and predict intervals affected by magnetite dissolutions. We also measured total sulfur content, grain size distributions, total organic carbon (TOC) content, and magnetic mineral assemblage. The upper 100 m of Site 1252 contains a short interval of κ driven by primary magnetite, with multiple intervals (> 90 m total) of decreased κ correlated with elevated sulfur content, consistent with dissolution of magnetite and re-precipitation of pyrite. In the upper 90 m of Site 1249, κ is almost entirely altered by diagenetic processes, with much of the low κ explained by a high degree of pyritization, and some intervals affected by the precipitation of magnetic iron sulfides. At Site 1325, κ between 0-20 and 51-73 mbsf represents primary mineralogy, and in the interval 24-51 mbsf, κ may be reduced due to pyritization. This integrated approach allows for a prediction of primary κ and the amount of κ loss at each site when compared to actual κ measurements. In the case of magnetite dissolution and full pyritization, these drawdowns in κ are supported by sulfur measurements, and the exposure times of magnetite to hydrogen sulfide can be modeled. The presence of methane and methane hydrates at these sites, as well as large variations in TOC content, suggest that the past migration rates of the SMT and variation in sulfate reduction rates may influence κ alteration along the Cascadia margin.

TABLE OF CONTENTS

EXECUTIVE SUMMARY

Magnetic susceptibility (κ) is a mixed signal in marine sediments, representing primary depositional and secondary diagenetic processes. Production of hydrogen sulfide via anaerobic oxidation of methane (AOM) at the sulfate-methane transition (SMT), and organoclastic sulfate reduction above the SMT can result in the dissolution of iron oxides, altering κ in sediments in methane gas and gas hydrate bearing regions. We investigated records of κ on the Cascadia margin (ODP Sites 1249 and 1252; IODP Site 1325) using a Zr/Rb heavy mineral proxy from XRF core scanning to identify intervals of primary detrital magnetic susceptibility and intervals and predict intervals affected by magnetite dissolution. We identify multiple intervals of diagenetically-reduced κ at three sites along the Cascadia margin, including two slope basins and a methane seep site. By utilizing a Zr/Rb heavy mineral proxy we isolate the primary detrital κ signal at these sites and derive the loss of κ. From the loss of κ we model the loss of magnetite and the gain of pyrite sulfur. Measurements of total sulfur confirm the calculated loss of κ and magnetite, and precipitation of pyrite. At ODP Site 1249 κ is completely diagenetically altered for the complete record, with loss of κ in non-greigite bearing intervals. The upper 100 m of Site 1252 contains a short interval of κ driven by primary magnetite, with multiple intervals (> 90 m total) of decreased κ correlated with elevated sulfur content, consistent with dissolution of magnetite and re-precipitation of pyrite. In the upper 90 m of Site 1249, κ is almost entirely altered by diagenetic processes, with much of the low κ explained by a high degree of pyritization, and some intervals affected by precipitation of magnetic iron sulfides. At Site 1325, κ between 0-20 and 51-73 mbsf represents primary mineralogy, and in the interval 24-51 mbsf, κ may be reduced due to pyritization. These altered intervals of κ are likely prolonged past positions of the SMT, that are potentially influenced by sedimentation rate, gas hydrate dissociation, variable TOC content, and upward advective flux of methane. Sites 1252 and U1325 show increased TOC content in intervals of low magnetic susceptibility, suggesting a possible influence of TOC on the depth of the SMT and the role of organoclastic sulfate reduction or microbial iron reduction due to organic matter variability.

We identify three potential limitations that guide the applicability of the heavy mineral proxy approach developed in this project. First, we highlight the importance of the availability of reference intervals of unaltered κ, in which a relationship between κ and Zr/Rb is established. Second, determination of magnetic mineral assemblage is important for the application of this method. The presence of magnetic iron sulfides presents a more complicated scenario compared to the full pyritization of magnetite. Our approach assumes a full reaction to stable paramagnetic pyrite rather than formation of ferrimagnetic iron sulfides Lastly, in coarse-grained sediments the relationship between κ and Zr/Rb is more uncertain compared to fine-grained sediments.

In summary, we demonstrate the applicability of an integrated approach to identify intervals of altered κ and confirm the sulfur-diagenetic source of the magnetic drawdowns along the Cascadia margin, and other sediments with magnetite-dominant magnetic assemblages. Our magnetic susceptibility and elemental profile approach allows for tracking of paleo-SMT positions which allows for interpretation of evolving methane hydrate systems over time.

REPORT DETAILS

Introduction

Magnetic susceptibility, measured as volume-dependent (κ) or mass-dependent (χ) magnetic susceptibility is a measure of the ratio of induced temporary magnetization to an applied field that is proportional to the quantity of ferromagnetic minerals in a material. Magnetic susceptibility is a widely-measured parameter applied to samples from sediment records to address a variety of environmental and diagenetic questions (e.g. Liu et al., 2012; Verosub and Roberts, 1995). Magnetic susceptibility is commonly measured in marine sediments, and κ is a standard measurement on Ocean Drilling Program (ODP) and Integrated Ocean Drilling Program (IODP) expeditions collected using a MSCL (multi-sensor core logger) (Blum, 1997). Downcore variation in magnetic susceptibility can represent a variety of marine sedimentary processes, including turbidite deposition (Goldfinger et al., 2012; Karlin and Abella, 1994; Kirby et al.,1998; Sager and Hall, 1990; Taira and Niitsuma, 1986), eolian transport (Bloemendal et al., 1992; Doh et al., 1988; Lowrie and Heller, 1982; Robinson, 1986), and ice-rafted debris (Hall and King, 1989; Richter et al., 2001; Stoner et al., 1995). These detrital patterns represent the accumulation of iron oxide minerals, such as magnetite (Fe_3O_4), hematite (Fe_2O_3), and goethite (αFeOOH) in marine sediments.

After deposition these magnetic iron oxides are subject to reaction with hydrogen sulfide produced during early diagenesis. In marine sediments, hydrogen sulfide is produced by sulfate-reducing bacteria via organoclastic sulfate reduction (Eq. 1) (e.g. Berner et al., 1970):

$$CH_2O + SO_4^{-2} \rightarrow H_2S + 2HCO_3^- \quad (1)$$

In addition, at the sulfate-methane transition (SMT) hydrogen sulfide is produced by a consortium of sulfate-reducing bacteria and methanotrophic archea (Eq. 2) (Boetius et al., 2000; Hinrichs et al., 1999; Hoehler et al., 1994) or by methanotrophic archaea alone (Milucka et al., 2012) (Eq. 3), during anaerobic oxidation of methane (AOM) (Reeburgh, 1976):

$$CH_4 + SO_4^{2-} \rightarrow HCO_3^- + HS^- + H_2O \quad (2)$$
$$7CH_4 + 8SO_4^{2-} + 5H^+ \rightarrow 4HS_2\text{-} + 7HCO_3^- + 11H_2O \quad (3)$$

Hydrogen sulfide reacts with dissolved iron and reactive iron minerals through multiple intermediate reaction steps to ultimately form pyrite (Berner, 1970, 1984; Rickard et al., 1995; Schoonen, 2004). Magnetite reacts readily with hydrogen sulfide to liberate iron and elemental sulfur (Eq. 4) (Pyzik and Sommer, 1981) which rapidly forms amorphous iron monosulfides, such as mackinawite (Eq. 5) (Berner, 1970; Pyzik and Sommer, 1981):

$$Fe_3O_4 + HS^- + 7H^+ \rightarrow 3Fe^{2+} + S^0 + 4H_2O \quad (4)$$
$$Fe^{2+} + HS^- \rightarrow FeS + H^+ \quad (5)$$

Further reaction of FeS to pyrite can occur via three possible mechanisms. These reactions include continued reaction with hydrogen sulfide (Eq. 6) (Rickard and Luther, 1997), addition of sulfur (Eq. 7) (Berner, 1970, 1984), and loss of iron (Eq. 8) (Wilkin and Barnes, 1996):

$$FeS + H_2S \rightarrow FeS_2 + H_2 \quad (6)$$
$$FeS + S^0 \rightarrow FeS_2 \quad (7)$$

$$2FeS + H^+ \rightarrow FeS_2 + Fe^{2+} + H_2 \quad (8)$$

Of these potential reactions, Eq. 6 is thermodynamically most likely, if hydrogen sulfide is present (Rickard, 1997).

Pyrite may also be formed from FeS via steps involving intermediate magnetic iron sulfides, such as greigite, which is a product of sulfur (polysulfide) and FeS (Eq. 9) (Sweeney and Kaplan, 1973):

$$3FeS + S^0 \rightarrow Fe_3S_4 \quad (9)$$

Similar to the reaction of FeS to FeS_2, greigite may experience further sulfidization via further reaction with hydrogen sulfide (Eq. 10) (Neretin et al., 2004), addition of sulfur (Eq. 11) (Sweeney and Kaplan, 1973), and loss of iron (Eq. 12) (Furukawa and Barnes, 1995):

$$Fe_3S_4 + 2H_2S \rightarrow 3FeS_2 + 2H_2 \quad (10)$$
$$Fe_3S_4 + 2S^0 \rightarrow 3FeS_2 \quad (11)$$
$$Fe_3S_4 + H^+ \rightarrow 2FeS_2 + Fe^{2+} + H_2 \quad (12)$$

Given the potential for dissolution of magnetic iron oxides and formation of diagenetic iron sulfides in marine sediments, interpretation of the primary magnetic mineral assemblage may be altered (e.g. Nilsson et al., 2013; Roberts and Turner, 1993). Diagenetic overprints of primary depositional κ signals in methane-bearing stratigraphy have been identified in a variety of marine sediment records (e.g. Kasten et al., 1998; Musgrave and Hiroki, 2000). Often magnetite content and magnetic grain size decreases with depth in the sulfate-reducing zone as sulfide solids increase (Karlin and Levi, 1985, Karlin, 1990) due to pyritization of magnetite (Canfield and Berner, 1987). A prolonged pause in upward SMT migration (Riedinger et al., 2005) or high sustained methane flux at a methane vent (Novosel et al., 2005) may produce reductions in κ via dissolution of ferromagnetic magnetite and precipitation of paramagnetic pyrite. Magnetic iron sulfides have been observed in gas hydrate settings (Housen and Musgrave, 1996; Larrasoaña et al., 2006, 2007; Musgrave et al., 2006), maintaining or increasing κ. Thus, κ records in methane-bearing stratigraphy represent a potentially-mixed detrital and diagenetic signal (Johnson et al., 2010). Zr/Rb as measured by X-ray fluorescence (XRF) has been utilized as a grain size proxy (Dypvik and Harris, 2001). More specifically, Zr/Rb is an indicator of heavy mineral content in the absence of grain size variation, and in unaltered hemipelagic sediments can be highly correlated with κ (Phillips et al., 2014). By using Zr/Rb to predict detrital κ, we can unravel the detrital and diagenetic components in the κ signal.

In this study, we investigate the source of magnetic susceptibility variation at in the upper 100 mbsf at three sites (Fig. 1) along the Cascadia accretionary wedge (ODP Sites 1252 and 1249; IODP Site U1325) to partition the κ signal into detrital and diagenetic components. These sites encompass a range in diagenetic environments from a methane vent site (ODP Site 1249) to two slope basin sites (ODP Site 1252 and IODP Site U1325) with lower methane flux and observed gas hydrate. Each site shows intervals of very low κ that may represent diagenetic dissolution, which is now below the modern SMT (Fig. 2). By accounting for predicted κ we estimate the loss of magnetite and pyrite sulfur precipitation to identify intervals of diagenetic alteration in these gas hydrate bearing records.

Geologic and Oceanographic Setting

The formation and continued evolution of the Cascadia accretionary wedge is a result of the oblique subduction of the Juan de Fuca, Gorda, and Explorer plates, where abyssal plain sediments are accreted and uplifted into a series of thrust ridges and slope basins. Abyssal plain sediments of these plates are dominated by turbidites and hemipelagic clays of the Astoria and Nitinat Fans. In the accretionary wedge, uplifted sediments on the structural highs, such as Hydrate Ridge are eroded and re-deposited in the slope basins with interspersed hemipelagic clay. Seismic reflection data across Hydrate Ridge sites (Tréhu et al., 2004) show the ridge is composed of uplifted and accreted abyssal plain fan sediments covered by various-age slope-basin sediments, which are in turn uplifted and deformed during the continued evolution of the wedge (Johnson et al, 2006).

Primary detrital magnetic susceptibility in Cascadia margin sediments is sourced by sediment transport to abyssal plain and subsequent uplift and re-deposition of ferromagnetic minerals. Erosion of magnetite and titanomagnetite-bearing Columbia River Basalts (Long and Wood, 1986) and Cascade Arc volcanism (Jicha et al., 2009) serve as potential provenance for magnetite delivered to the continental shelf. These sediments are transported to the abyssal plain through turbidites and other mass flows, often through established submarine canyons e.g., through Astoria Canyon to the Astoria Fan, and through the Barkley and Juan de Fuca Canyons to the Nitinat Fan. Magnetite is commonly observed in sediments of abyssal fans and in the accretionary complex (Chamov and Murdmaa, 1995).

Marine organic matter along this margin is sourced by primary productivity that is influenced by the dynamics associated with the splitting of the North Pacific current into the Callifornia Current and the Alaska Current. Phytoplankton production in the southern Cascadia region is primarily driven by Ekman-driven coastal upwelling associated with the California current (Lynn and Simpson, 1987), the southward flowing component of the North Pacific Gyre. In spite of the downwelling nature of the Alaska current, the northern Cascadia region remains productive, due to upwelling driven by mesoscale eddies (Peterson et al., 2005) and injection of nutrient-rich bottom water to the continental shelf during summer weakening of the Alaska current (Childers et al., 2005). Along the southern Cascadia margin, productivity and TOC accumulation are likely driven by the California Current, which is influences productivity on glacial-interglacial and suborbital timescales further to the south along the California margin (Gardner et al., 1997).

TOC measured along the Cascadia margin is a mixture of marine and terrestrial organic matter (Prahl et al., 1994; Kim and Lee, 2009). The terrestrial component is highest on the continental slope (mean δ^{13}TOC=-23.9‰), and decreases to the continental slope and abyssal plain (mean δ^{13}TOC=-21.8‰ and -21.4‰ respectively) along the Washington margin (Prahl et al., 1994). TOC generally increases at the slope and abyssal plain compared to the shelf. At sites along the Northern Cascadia margin, δ^{13}TOC is generally more depleted (-24 to -26‰) and the most landward sites of the IODP Exp. 311 transect, have slightly less depleted δ^{13}TOC indicating the highest marine organic matter component (Kim and Lee, 2009). The differences between these sites suggest that TOC content and source vary along the slope depending on terrigenous flux and surface biological productivity, as observed on most continental margins (e.g. Johnson et al., 2014).

Site 1249 is located at the summit of southern Hydrate Ridge in 775 m water depth (Shipboard Scientific Party, 2003a) in a region of observed seafloor gas hydrate and methane venting (Heeschen et al., 2003, 2005; Suess et al., 1999, 2001). Unit I in the upper 51.5 m of Site

1249 is comprised of nannofossil- and diatom-bearing silty clay and diatom-rich silty clay. Unit II, between 51.5 and 90 mbsf is characterized by diatom-bearing to –rich silty clay, with intervals of nannofossil-bearing to –rich silty clay, and minor turbidite lithologies. Mousselike and soupy textures are common throughout Site 1249 representing the dissociation of disseminated and massive gas hydrate (Shipboard Scientific Party, 2003a). Iron sulfides were commonly observed throughout Site 1249 cores, and iron sulfide nodules and authigenic carbonate-rich clay were also observed.

The absence of sulfate and presence of methane at the seafloor at Site 1249 indicates direct flux of methane to the seafloor with an SMT at the sediment surface (Shipboard Scientific Party, 2003a). Observations of Beggiatoa microbial mats and seafloor AOM (Boetius et al., 2000) and methane-derived authigenic carbonates (Bohrmann et al., 1998; Greinert et al., 2001; Ritger et al., 1987; Suess et al., 1999) at Hydrate Ridge suggests Site 1249 is representative of widespread methane expulsion imaged as near seafloor authigenic carbonates across the crest of Hydrate Ridge by sidescan sonar (Johnson et al., 2003). Positive chloride anomalies in pore waters at Site 1249 suggest formation of gas hydrate and subsequent brine formation at rates faster than removal by diffusion or advection (Shipboard Scientific Party, 2003a). Enhanced salinity due to hydrate formation promotes a three-phase equilibrium between methane hydrate, dissolved methane, and water, and allows methane to be transported through the gas hydrate stability zone (Liu and Flemings, 2006).

Site 1252 is located in a slope basin approximately 4.5 km NE of the southern Hydrate Ridge summit in 1040 m water depth (Shipboard Scientific Party, 2003b). Unit I (upper 96.4 mbsf) is comprised of diatom-bearing to –rich silty clay. There is a regional unconformity at 96.4 mbsf and Unit II (96.4 -113.9 mbsf) is foraminifer-rich silty clay punctuated by layers of upward-fining turbidites. Unit III (113.9-259.8 mbsf) is comprised of silty clay with sandy silt turbidites. Iron sulfide mottles and nodules were commonly observed at this site. Sulfate decreases linearly to the SMT at approximately 5 mbsf (Shipboard Scientific Party, 2003b) and methane is present in headspace samples below the SMT. Distinct chloride anomalies were not observed at Site 1252, but cold anomalies were observed at 83 and 99 mbsf (Shipboard Scientific Party, 2003b).

Site U1325 is located in 2195 m water depth in the first slope basin landward of the deformation front on the primary transect drilled by IODP Expedition 311 (Expedition 311 Scientists, 2006). Unit I (0-52.2 mbsf) is comprised of silty clay containing diatoms, and sand layers ranging from mm to m in thickness. Unit II (52.2-102.3 mbsf) is comprised of silty clay and clayey silt interbedded with sand, silty sand, and sandy silt. Iron sulfide mottling and concretions are common throughout these records. The SMT is located between 4 and 5 mbsf at Site 1325 (Expedition 311 Scientists, 2006). Freshened chloride anomalies below 70 mbsf indicate the dissociation of gas hydrate upon core recovery.

Experimental Methods

Sediment core sections from Sites 1249, 1252, and U1325 were scanned at a 4 cm resolution using an Avaatech X-ray fluorescence (XRF) core scanner at Texas A&M University. The 4 cm measurement interval was adjusted in some intervals to avoid expansion cracks or moussey/soupy textures. XRF scanning was conducted at 10 kV (no filter), 25 kV, (Pd filter), and 50 kV (Cu filter) energy levels. Elements measured include Zr, Rb, S, Fe, Ti, Ba, and Br

(see Table 1 for full list). Normalized ratios of XRF Fe to κ (Hepp et al., 2009) were calculated to identify which intervals with abundant paramagnetic iron minerals (e.g. pyrite).

Grain size distributions of discrete sediment samples (~0.5 cm^3 of sediment approximately every 1 m) were measured for Sites 1249, 1252, and U1325 using a Malvern Mastersizer 2000 laser diffraction particle size analyzer and Hydro 2000G dispersal unit at the University of New Hampshire. Bulk samples were measured, as well as samples treated with 10 mL of 10% HCl and 15 mL of 30% H_2O_2 to remove carbonate and organic matter. The grain size distributions were used to calculate median, 10% and 90% grain size classes, and sand, silt, and clay-sized fractions.

Approximately 1 g of sediment was dried at 50 ° C, crushed and 10 mg subsamples were run using a Perkin Elmer 2400 Series CHNS/O Analyzer at the University of New Hampshire. Splits of untreated powder were used for total CHNS analysis and splits of 6% sulfurous acid-treated samples were run for TOC according to the procedures in Phillips et al. (2011). Duplicate samples were analyzed approximately every 10 samples. Inorganic carbon (IC) was calculated by the subtraction of TOC from total carbon (TC), and $CaCO_3$ was calculated by multiplying IC by 8.333. TOC/TN was calculated as TOC/TN = (TOC/12.011)/(TN.14.007).

A subset of powdered samples were analyzed for $\delta^{13}C$ of TOC ($\delta^{13}TOC$) at Washington State University using a Costech ECS 4010 elemental analyzer interfaced with a Thermofinnegan Delata Plus XP continuous flow isotope ratio mass spectrometer. $\delta^{13}TOC$ results are presented relative to the Vienna Pee Dee belemnite (VPDB) in per mil (‰).

To complement existing rock magnetic datasets at Sites 1249 and 1252 (Larrasoaña et al., 2006, 2007), we measured mass-dependent magnetic susceptibility (χ) and isothermal remanent magnetism (IRM) in samples from Site U1325 in the Paleomagnetism Laboratory at the University of New Hampshire. Sediment samples were measured for χ using a Bartington MS2 Magnetic Susceptibility System. Samples were then cut into 1 cm^3 cubes, wrapped in foil, and subjected to stepwise acquisition of IRM with subsequent thermal demagnetization following the method of Lowrie (1990). IRM was acquired in steps from 0 to 1100 mT, with backfield magnetizations at -100 mT and -300 mT, using an ASC Scientific IM-10-30 Impulse Magnetizer. Remanent magnetizations were measured using an HSM2 SQUID-based Spinner Magnetometer. Thermal demagnetization was conducted in steps from 25 to 680 °C using an ASC Scientific TD-48 Thermal Demagnetizer.

Samples for rock magnetic analyses are typically sampled immediately after coring, sealed under nitrogen gas, and frozen until analysis. In this study, we attempted to measure magnetic properties on samples from cores stored at 4 °C and sealed under atmospheric conditions for approximately 8 years at the IODP Gulf Coast Repository since collection during IODP Expedition 311 in September 2005. Comparison between original shipboard magnetic susceptibility and measurements we performed in the lab at UNH are similar, thus oxidation of magnetic minerals since core collection for the cores uitlized in our study has not been significant.

Samples for $\delta^{18}O$ and $\delta^{13}C$ isotopic analysis of foraminiferal carbonate (20 cm^3 of sediment) were freeze dried at -48 °C and 0.006 kPa for 24 h, and dispersed in 1 L of 5 g/L sodium hexametaphosphate ($(NaPO_3)_6$) solution. The dispersed samples were shaken on a wrist-action shaker for 3 h and then sieved through 63 μm sieves. From this coarse fraction, benthic foraminifer species *Uvigerina peregrina, Bulimina mexicana,* and *Globobuliminia pacifica* were selected for $\delta^{18}O$ and $\delta^{13}C$ isotopic analysis. Initial sampling focused on *Uvigerina peregrina* and were measured for $\delta^{18}O$ and $\delta^{13}C$ using a Finnegan MAT 252 isotope ratio mass spectrometer with Kiel III device at the Oregon State University Stable Isotope Laboratory. Due to intervals lacking *Uvigerina peregrina* or low general abundance of benthic foraminifers, additional samples of *Bulimina mexicana,* or *Globobuliminia pacifica.* were selected and measured using a Finnegan MAT 253 isotope ratio mass spectrometer with Kiel IV device at the University of Michigan Stable Isotope Laboratory.

We predict detrital κ using the relationship of a Zr/Rb magnetic mineral proxy at each site, quantified by regression analysis for best fit and 95% prediction intervals. Intervals in which there is a strong correlation between Zr/Rb and κ were used for regression analysis. At Site 1252 there is strong correlation between Zr/Rb and κ between 75 and 80 mbsf, that is assumed to represent an interval in which κ is unaltered by diagenesis. Additional XRF core scans between 0 and 13 mbsf at Site 1251 were combined in the Zr/Rb vs. κ regression analysis to strengthen the understanding of the κ-Zr/Rb relationship at Hydrate Ridge. At Site U1325 separate regressions were analyzed for the intervals 4.5-20 mbsf and 51 to 73 mbsf.

By subtraction of measured κ from predicted κ we estimate the loss of magnetic susceptibility. Based on the results of IRM analysis demonstrating magnetite as the dominant detrital remanence-carrying mineral, we used of a κ value of 1,000,000 x 10^{-6} SI for pseudo single domain (PSD) magnetite (Hunt et al., 1995) to estimate magnetite content. This value of PSD magnetite κ (0.001 mass fraction magnetite = 1,000 x 10^6 SI) is used for calibration of ODP/IODP κ measurements (Blum, 1997). Assuming dissolution of magnetite and complete reduction to pyrite, we calculate sulfur precipitation in wt. % based on a stoichiometric ratio of 1.12 mol of pyrite S produced for every 1 mol of magnetite iron reduced.

Additionally, we estimate the amount of time in years necessary for reaction with hydrogen sulfide to account for the observed magnetite loss using the rate equation developed by Canfield and Berner (1987):

$$\frac{dC_{mag}}{dt} = -1.1x10^{-5}C_s^{0.5}C_{mag}A_{mag}$$

where C_{mag} is the magnetite concentration (g magnetite/g sediment), C_s is the concentration of dissolved sulfide (mM) and A_{mag} is the surface area of magnetite (cm^2/g magnetite). Magnetite concentration at the time of deposition was estimated from the record of predicted κ using the relationships described in Section 3.5. Peak hydrogen sulfide values of 1.6 mM and 3.6 mM at Sites 1249 and 1252 respectively (Borowski et al., 2006) were used for C_s. Hydrogen sulfide measured at Site 1325 is not available, and the peak value from Site 1252 was used, due to its similar slope basin setting. We assume a surface area of 660 cm^2/g magnetite, the average from Canfield and Berner (1987). Mean bulk density over the applicable intervals at each site were

used to scale the estimated time of magnetite loss based on g of sediment to cm^3 of sediment for discussion relative to down hole depths.

Results

At Site 1249, median grain size varies between 8 and 12 μm, with coarser samples at 41.44 and 86.09 mbsf (13.5 and 18.1 μm respectively) (Fig. 3). Zr/Rb varies between 1.2 and 1.8, and Ti/Rb varies between 2.1 and 3.1 (Fig. 3). There is strong correlation between Zr/Rb and Ti/Rb, but little correlation between these proxies and median grain size. There is poor correlation between κ (Shipboard Scientific Party, 2003) and the XRF proxies. Measurements by Larrasoaña et al. (2006) demonstrate that much of the magnetic assemblage at Site 1249 is dominated by magnetite, with intervals of magnetic iron sulfide-dominant assemblages at 49.55, 69.93, and 86.01 mbsf.

At Site 1252, median grain size varies between 8 and 13 μm. Zr/Rb varies between 1.2 and 1.5, and Ti/Rb varies between 1.6 and 1.9 (Fig. 4). Similar to Site 1249, there is strong correlation between Zr/Rb and Ti/Rb, but there is little correlation between these proxies and median grain size. For most of the record there is poor correlation between κ (Shipboard Scientific Party, 2003) and the XRF proxies, except between 75 and 80 mbsf. Previous work demonstrates that the magnetic assemblages at all depths at Site 1252 are dominated by magnetite (Larrasoaña et al., 2006).

In the upper 26 m of Site U1325, median grain size varies from 10 to 113 μm, with a consistently finer interval (9 to 17 μm median grain size) between 26 and 81 mbsf (Fig. 5). At 83.5 and 86.2 mbsf median grain size increases to 22.5 and 21.4 μm respectively. In the upper 20.2 mbsf at Site U1325, Zr/Rb exhibits the largest variability ranging from 1.0 to 8.6 (Fig. 5). Between 24 and 52.5 mbsf, Zr/Rb is less variable, ranging between 0.9 and 3.8. Zr/Rb increases in the interval between 54 and 73 mbsf, ranging between 1.1 and 5.9. Ti/Rb displays a down core pattern similar to Zr/Rb. Ti/Rb varies between 1.9 and 6.6 in the upper 20 mbsf, between 1.4 and 3.0 in the 24-52.5 mbsf interval, and 1.5 and 3.6 in the interval 54-73 mbsf. There is a strong correlation between κ and Zr/Rb and Ti/Rb proxies between 4.5 and 20 mbsf, and between 51 and 74 mbsf. IRM measurements indicate that magnetite dominates the magnetic mineral assemblage throughout most of the record at Site U1325, with samples of mixed magnetite and magnetic iron sulfides at 43.10, 66.60, and 75.32 mbsf (Fig. 5)

Using observed intervals in Sites 1252 (with additional data from Site 1251) and Site U1325, where there is good correlation between Zr/Rb and κ, we used regression analysis to predict best fit and 95% prediction intervals. At Sites 1252/1251, there is an overall linear relationship between Zr/Rb (ranging from 1.3 to 1.8) and κ (ranging from 15 to 211 SI x 10^{-7}) with an r^2 value of 0.76 (Fig. 6). At Site U1325, separate regression for the intervals 4.59-18.80 mbsf and 51-73 mbsf show a wider range in Zr/Rb and κ than at Site 1252, and are best fit by a logarithmic function. Between 4.59 and 18.80 mbsf, Zr/Rb varies from 1.0 to 8.6 and κ varies from 46.4 to 315 SI x 10^{-7}.

At Site 1249, predicted detrital κ is significantly higher than measured κ for much of the record (demonstrated by 95% prediction intervals), except for the intervals 34.5-54.4 mbsf and 65.1-88.0 msbf (Fig. 7). Actual κ varies from 2.0 to 44.3 SI x 10^{-7} (mean: 25.0), while best-fit predicted κ varies from 5.7 to 114.5 SI x 10^{-7} (mean: 49.3). Intervals in which predicted κ is not higher than actual κ have samples that the magnetic mineral assemblage is magnetic sulfide dominant (Larrasoaña et al., 2006). The maximum predicted loss of κ of 63 SI x 10^{-7} is predicted in the upper 29 mbsf and up to 84 SI x 10^{-7} in the interval between 54 and 75 mbsf. This loss of κ corresponds to dissolution of up to 0.8 wt. % magnetite, and precipitation of up to 0.7 wt. % S. Measured S varies from 0.11 to 0.7 wt. %. Fe/κ is relatively consistent over the upper 49 mbsf, and below a peak at 50 mbsf, Fe/κ decreases and is more variable between 50 and 88 mbsf. TOC falls in the range of 0.80 to 1.76 wt%, and XRF-measured Br correlates to the downcore pattern in TOC. TOC/TN varies between 6.6 and 10.2 and δ^{13}TOC varies from -23.3 to -22.8 ‰ VPDB.

At Site 1252, predicted κ is higher than measured for most of the upper 100 mbsf except for the interval 75-78 mbsf (Fig. 8). Actual κ varies from 10.9 to 158.8 SI x 10^{-7} (mean: 26.4) while best-fit predicted κ varies from 22.3 to 141.7 SI x 10^{-7} (mean: 72.8). The intervals with the highest predicted loss of κ and magnetite are 0-28.8, 31.8-41.7, 45.3-54.4, 58.5-70.9, and 78.2-101.3 mbsf. In these intervals, average predicted κ loss and magnetite loss is 48.6 SI x 10^{-7} and 0.49 wt% respectively. Average predicted precipitated S gain in these intervals is 0.39 wt. %. Overall, measured S matches the downcore pattern in predicted S, with a notable mismatch between 45 and 52 mbsf. Mean measured S is 0.42 wt. %, varying from 0.29 to 0.72 wt. %. Normalized Fe/κ increases distinctly in the intervals of highest predicted loss of magnetite (Fig. 8). TOC is relatively high with a mean of 1.53 wt. % and variable, ranging from 1.05 to 2.18 wt. %. Increases in TOC occur in the intervals with highest magnetite loss and S gain. Average TOC/TN is 8.8 and increase in intervals of elevated TOC. δ^{13}TOC varies from -23.8 to -22.3 becoming less depleted in higher TOC intervals.

At Site U1325, predicted κ matches measured κ closely in the upper 20 mbsf and between 54-73 msbf (Fig. 9). Predicted detrital κ is significantly higher than measured κ over the intervals 24.2-43.7 and 44.1-51.4 mbsf. Likewise, there is average κ loss of 154.7 SI x10-7 and 1.5 wt. % average magnetite loss over this interval. Best fit S precipitation gain on average is 1.25 wt. % over the interval of κ loss, while average measured S is 0.39 wt. %, with the overall pattern of measured S following predicted S. Fe/κ is elevated from 1.5-2.1, 24.5- 57.2, and 69.3-76.8 mbsf. TOC is highly variable downcore, ranging from 0.07 to 1.73 wt. %. Distinct increases in TOC occur in the upper 10, 15-43, and 71-79 mbsf. Increases in TOC match decreases in TOC/TN and increases in δ^{13}TOC (Kim and Lee, 2009).

Estimated time in years per cm^3 sediment for observed magnetite dissolution at the SMT hydrogen sulfide peak varies following as the same pattern as predicted κ loss (Fig. 10). At Site 1249, the time for dissolution averages at 80 years/cm^3 with maximum of 235 years/cm3. There are short intervals of zero or negative time, which likely represent intervals containing magnetic iron sulfides. At Site 1252, the average time for magnetite dissolution is 62 years with a maximum of 83 years/cm3. In intervals where predicted κ matches measured κ, predicted time is

near-zero or slightly negative. At Site U1325, considerably negative time is predicted in intervals of high Zr/Rb where there is poor prediction of detrital κ. In intervals of lower Zr/Rb (between 24 and 51 mbsf), average time is 122 years/cm3 with a maximum of 181 years/cm3.

Discussion

Assessing our Approach

Throughout this project we developed several new approaches and through sensitivity testing can now evaluate the limits of our methods. The first limitation to using Zr/Rb as a heavy mineral proxy to predict magnetic susceptibility is having intervals of original, unaltered κ that can be measured with XRF core scanning for Zr and Rb and used to establish a relationship between Zr/Rb and κ. Unaltered intervals, or nearby reference sites, in which κ matches the record of Zr/Rb are necessary to establish the relationship used to predict the detrital κ pattern. Thus, without the lower flux Sites 1252, 1251, and U1325, we would be unable to predict κ and estimate loss of magnetite at Site 1249, in which κ appears to be entirely overprinted by diagenetic dissolution. The relationship between κ and Zr/Rb is consistent between the Hydrate Ridge Sites 1251/1252 and Northern Cascadia Site U1325 (Fig. 6); however, this relationship likely is influenced by the mineralogical composition of the heavy mineral fraction (e.g. relative content of zircon vs. magnetite) and may vary over broader regional scales.

A second limitation is the dominant mineralogy used to estimate the amount of magnetic mineral loss. At these Cascadia margin sites, detrital mineralogy is dominantly magnetite (Larrasoaña et al., 2006), allowing for a straightforward relationship between κ and magnetite content (Hunt et al., 1995). With a complete pyritization of magnetite (e.g. Canfield and Berner, 1987), a clear decrease in κ would be observed (e.g. Novosel et al., 2005; Riedinger et al., 2005). However, in the case that intermediate ferrimagnetic iron sulfide minerals, such as greigite or pyrrhotite are formed after dissolution of magnetite (e.g. Housen and Musgrave, 1996; Larrasoaña et al., 2007; Musgrave et al., 2006), κ could be increased, maintained, or otherwise only minimally decreased compared the complete reaction to paramagnetic pyrite. At Site 1249, 34.5-54.4 and 65.1-88.0 msbf predicted detrital κ and measured κ are not significantly different, yet there is no correlation between κ and Zr/Rb. In this case, the presence of magnetic iron sulfides in these intervals (Fig. 3) (Larrasoaña et al., 2006) suggests that κ is higher than predicted given an assumption of complete reaction of magnetite to pyrite. At sites where a variety of depositional processes (fluvial, eolian, ice-rafted debris, volcanogenic) result in sediment records in which κ is strongly influenced by hematite and/or goethite content in addition to magnetite (e.g. Bloemendal et al., 1992;1993), additional quantification of magnetic mineral assemblage would be necessary.

A third limitation demonstrated by the record in upper 20 m of Site U1325 is the relationship of Zr/Rb and κ, and the relationship between κ and magnetite content in coarse sediments. Despite a consistent detrital magnetic mineral assemblage of magnetite, the linear relationship of Zr/Rb and κ becomes logarithmic and the correlation weakens above Zr/Rb of 2 (Fig. 6). In this case, Zr/Rb generally corresponds to a median grain size of greater than 20 μm

(Fig. 11). This suggests either (1) a possible increased variability and decreased content of heavy mineral composition in coarse sediments derived from turbidity currents or (2) the increased prevalence of multi-domain magnetite relative to single-domain or pseudo-single domain magnetite. In turbidites and other mass-transfer deposits, high-energy transport of sand-sized quartz and lithic grains may dilute magnetite content compared to the clay/fine silt hemipelagic mud. Additionally, variable sorting may result in an inconsistent relationship between zircon (driver of the Zr/Rb signal) and magnetite (driver of the κ signal) in these intervals. The presence of sand-sized, lithic grains may contain larger multi-domain magnetite which may have a decreased and variable κ response due to cancellation of magnetic moments in adjacent domains.

Zones with Depleted Magnetic Susceptibility

After establishing and accounting for the limitations of our approach and methods, we can interpret the source of the drawdowns of κ as the diagenetic dissolution of magnetite in the presence of H_2S and precipitation of sulfides. Although some intervals are likely influenced by the presence of greigite or pyrrhotite (as discussed in above), the magnetite-dominant assemblages suggest that magnetic susceptibility loss is mostly balanced by precipitation of pyrite. Because marine organic matter has an S/C ratio of approximately 0.02 (Suits and Arthur, 2000), the contribution of sulfur from organic matter is between <0.01 and 0.03 wt. % in sediment samples from these sites. Mean TS at these Sites 1249, 1252, and U1325 are 0.26, 0.42, and 0.30 respectively, suggesting that the vast majority of TS is derived from post-depositional precipitation.

At all three sites there are distinct intervals in which κ is less than predicted, while TS and Fe/κ is elevated (Fig. 7-9). This relationship demonstrates that magnetite loss is balanced by sulfur gain that suggests precipitation by pyrite, thus replacing a ferromagnetic mineral with paramagnetic mineral. Measured TS falls within the range of pyrite S gain predicted from κ dissolution. Possible mechanisms include AOM or organoclastic sulfate reduction due to the production of H_2S that can react with iron oxides to produce iron sulfides.

At Sites 1252 and U1325 there is a strong correlation of TOC with κ loss, TS, and Fe/κ (Fig. 8 and 9), which may suggest an increased intensity of organoclastic sulfate reduction and dissolution of magnetite in these intervals. Additionally, sediments with low TOC have been observed to have enhanced methane oxidation capacity (Pohlman et al., 2013), thus records such as Sites 1252 and U1325 which experience fluctuations in TOC greater than 1 wt. % may experience variations in depths of the SMT and rates of AOM. The intervals of κ loss may represent past prolonged positions of the SMT.

At Site 1249, there is little to no correlation between TOC and κ loss, TS, and Fe/κ. Because Site 1249 is a methane vent site located on the ridge, with observed gas hydrate (Shipboard Scientific Party, 1993), the reduced κ is likely due to sustained high methane flux and AOM (e.g. Novosel et al., 2005). This record indicates intervals of magnetic susceptibility loss and sustained or increased κ due to magnetic iron sulfides (Larrasoaña et al., 2006).

While our method clearly shows the presence of pyritization of magnetite by decreased κ and increased TS, identifying the specific biologeochemical processes responsible for these observations requires further work by additional modeling or proxies. Sedimentation rate influences the exposure time of magnetite in the sulfidic zone, potentially stalling or accelerating SMT migration (e.g. Riedinger et al., 2005) and changes in sedimentation rate may explain the reductions in κ observed in these records. Reactive transport models incorporating the dissolution of magnetite by reaction to H_2S and sedimentation rate might illuminate the role of organoclastic sulfate reduction or AOM in influencing these κ records. Measurement of $\delta^{34}S$ of pyrite as an indicator of sulfur limitation (e.g. Peketi et al., 2012; Borowski et al., 2013) could suggest whether sulfide-rich, reduced κ intervals are a result of near-seafloor organoclastic sulfate reduction or AOM at the SMT.

Estimating Hydrogen Sulfide Exposure Time

Predicting magnetite loss and sulfur precipitation allows for constraints on the amount of time for reaction with hydrogen sulfide to occur. At these sites we estimate that the duration of exposure to 1.6 to 3.6 mM HS^- (maximum measurements at the SMT) necessary to produce the predicted losses in κ at Sites 1249, 1252, and U1325 to be on the order of multiple decades to several centuries. These constraints can provide a basis for testing the influence of sedimentation rate on diagenetic drawdowns in κ. Because the SMT is an ephemeral redox boundary that can be influenced by sedimentation rate (e.g. Hensen et al., 2003), stagnation of the SMT can allow for increased exposure of magnetite to AOM-produced hydrogen sulfide and decreases in κ (Riedinger et al., 2005). Using the range in sedimentation rates used to explain the drawdown in κ by Riedinger et al. (2005) we can interpret the feasibility of constraining our approach using sedimentation rates. Assuming no change in methane flux, under steady state sedimentation, we would expect the SMT to migrate upward in pace with sedimentation rate. In a high-sedimentation rate scenario (100 cm/kyr), the peak of hydrogen sulfide at the SMT, and any portion of the hydrogen sulfide profile, would move through 1 cm of the sediment column over 10 years. Under a slow-sedimentation rate situation (5 cm/kyr), the SMT would take 200 years to migrate through 1 cm of sediment.

Sites 1249, 1252, and U1325 require on average 60 to 120 years of exposure to hydrogen sulfide concentrations typical of the SMT to explain loss of κ in a 1 cm section of sediment, which is on the same order as the exposure time to the peak of the SMT based on the sedimentation rates discussed above. Due to diffusion and organoclastic sulfate reduction, hydrogen sulfide can exist several meters or more above and below the SMT. Thus, further work utilizing a reactive transport model constrained by sedimentation rates, porosity, and rates of AOM and sulfate reduction can determine whether sedimentation rate can explain the observed drawdowns in κ. Initial benthic foraminifer oxygen isotope records indicate a slower and more uniform sedimentation rate at Site 1249 compared to Sites 1252 and U1325 (Fig. 12). By confirming or eliminating the influence of sedimentation rate, the remaining influence on depth of the SMT, methane flux, can be inferred.

Conclusions

We identify multiple intervals of diagenetically-reduced κ at three sites along the Cascadia margin, two in slope basins and one at a methane seep site. By utilizing a Zr/Rb heavy mineral proxy we isolate the primary detrital κ signal at these sites and derive the loss of κ. From the loss of κ we model the loss of magnetite and the gain of pyrite sulfur. To confirm the calculated loss of magnetite and pyrite precipitation, we measured total sulfur to confirm the diagenetic loss of κ. At ODP Site 1249 κ is completely diagenetically altered for the complete record, with loss of κ in non-greigite bearing intervals. At ODP Site 1252, there are repeated drawdowns in κ that are associated with increases in sulfur. Similarly, at IODP Site U1325 an interval of diagenetically altered magnetic susceptibility is balanced with increased sulfur content. These altered intervals of κ are likely prolonged past positions of the SMT, that are influenced by sedimentation rate, gas hydrate dissociation, TOC content, and advective fluid flow.

In addition, we identify three potential limitations that guide the applicability of the heavy mineral proxy approach. First, we highlight the importance of the availability of reference intervals of unaltered κ, in which a relationship between κ and Zr/Rb is established. Second, determination of magnetic mineral assemblage is important for the application of this method. The presence of magnetic iron sulfides presents a more complicated scenario compared to the full pyritization of magnetite. Lastly, in coarse-grained sediments the relationship between κ and Zr/Rb is more uncertain compared to fine-grained sediments.

In summary, we demonstrate the applicability of an integrated approach to identify intervals of altered κ and confirm the sulfur-diagenetic source of the magnetic drawdowns along the Cascadia margin, and our approach is applicable to other sediments with magnetite-dominant magnetic assemblages. Our magnetic susceptibility and elemental profile approach allows for tracking of paleo-SMT positions which allows for interpretation of evolving methane hydrate systems over time.

GRAPHICAL MATERIALS LIST

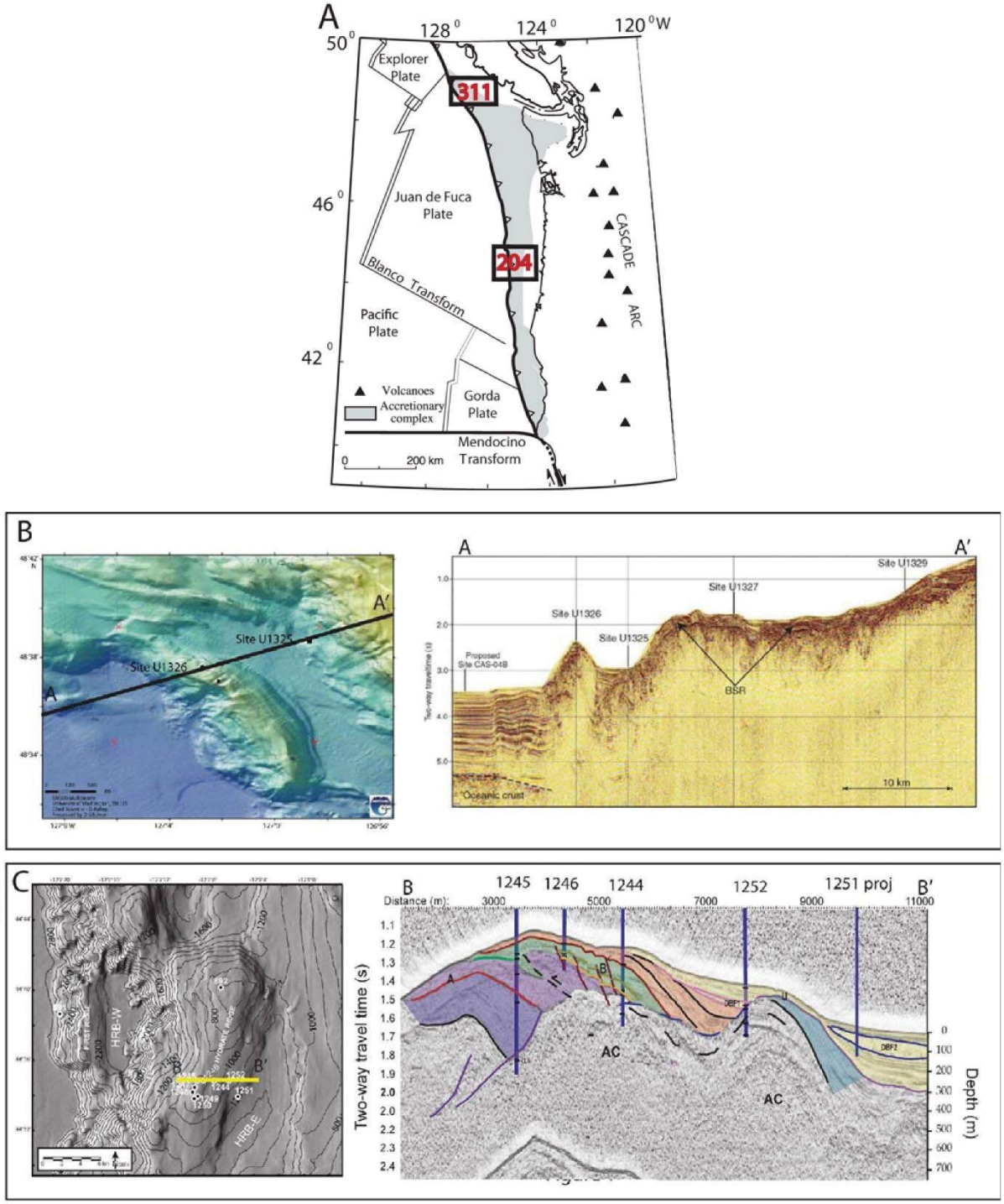

Figure 1. A. Location of IODP Exp. 311 and ODP Leg 204 drilling sites along the Cascadia margin. B. Multibeam bathymetry and seismic section across the Exp. 311 sites, notice site U1325 in the slope basin. C. Multibeam bathymetry and seismic secton across the Hydrate Ridge region. Notice site 1249 near the crest of southern Hydrate Ridge and Site 1252 in the adjacent slope basin to the east.

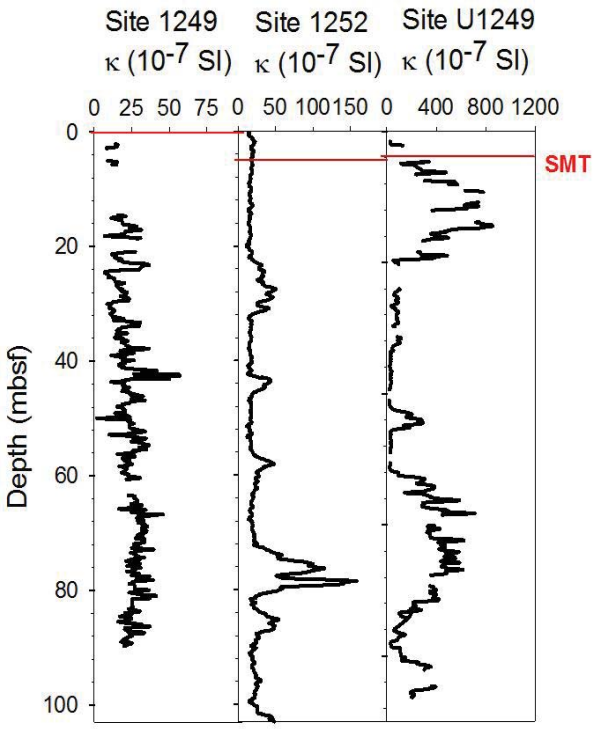

Figure 2. Magnetic susceptibility profiles at ODP Hole 1252A, ODP Holes 1249BCDF, and IODP Hole U1325B, shown with the depth of the modern SMT. κ and SMT depth from Shipboard Scientific Party (2003a,b) and Expedition 311 Scientists (2006).

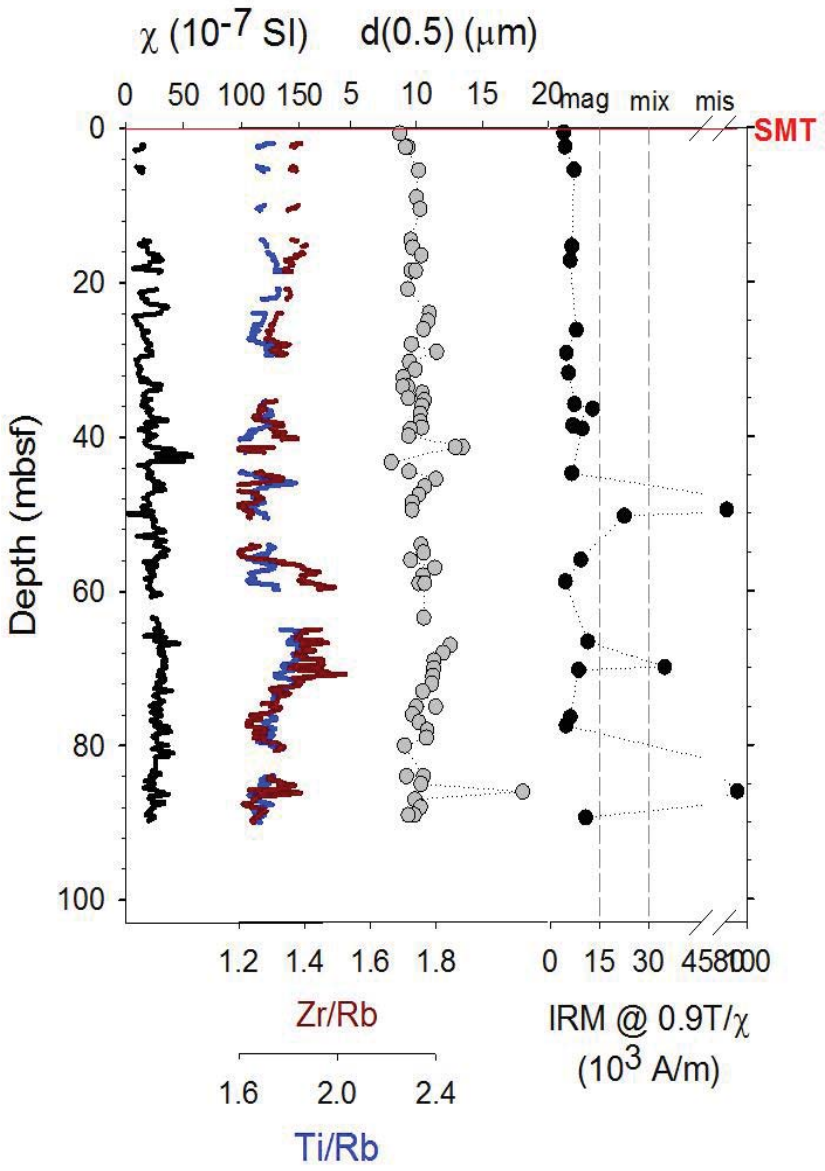

Figure 3. Magnetic susceptibility (κ), XRF Zr/Rb, XRF Ti/Rb, median grain size, and IRM @ 0.9/χ from ODP Holes 1249BCDF. κ from Shipboard Scientific Party (2003a) IRM from Larrasoaña et al. (2006).

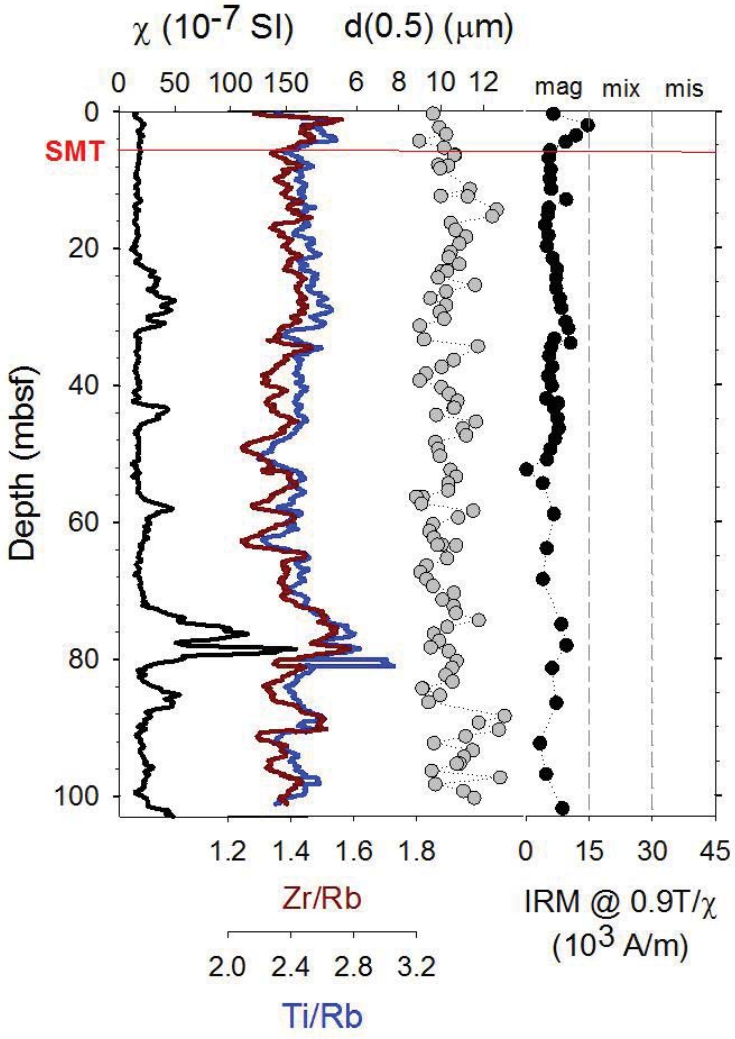

Figure 4. Magnetic susceptibility (κ), XRF Zr/Rb, XRF Ti/Rb, median grain size, and IRM @ 0.9/χ from ODP Hole 1252A. κ from Shipboard Scientific Party (2003a) IRM from Larrasoaña et al. (2006).

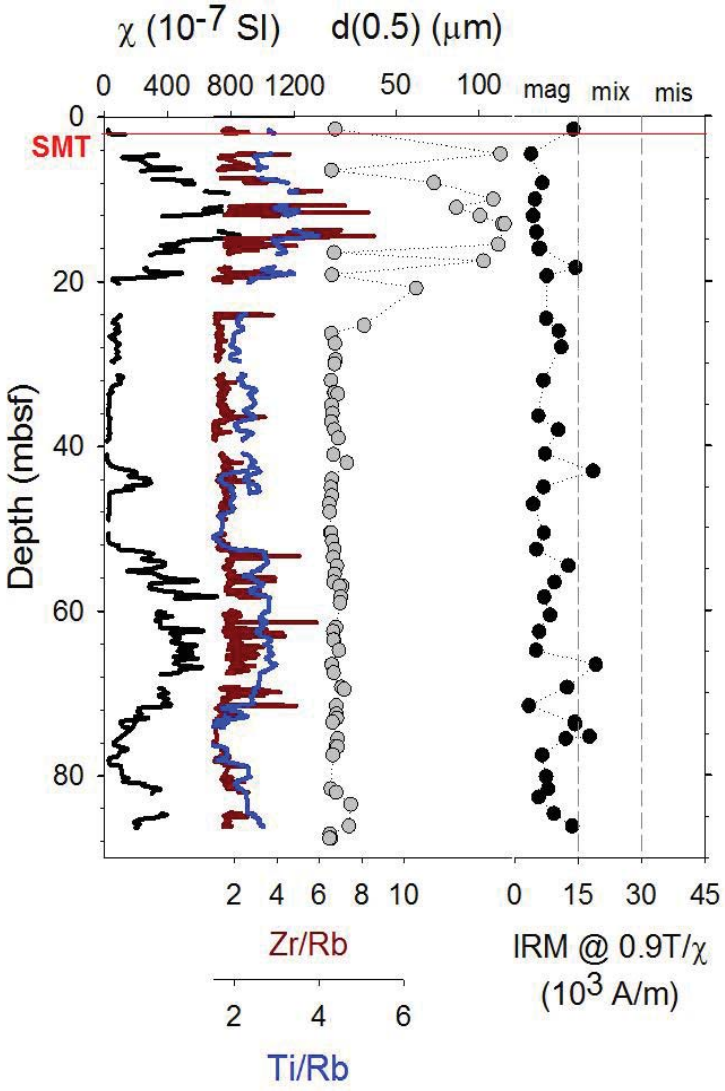

Figure 5. Magnetic susceptibility (κ), XRF Zr/Rb, XRF Ti/Rb, median grain size, and IRM @ 0.9/χ from ODP Holes U1325B. κ from Expedition 311 Scientists (2006).

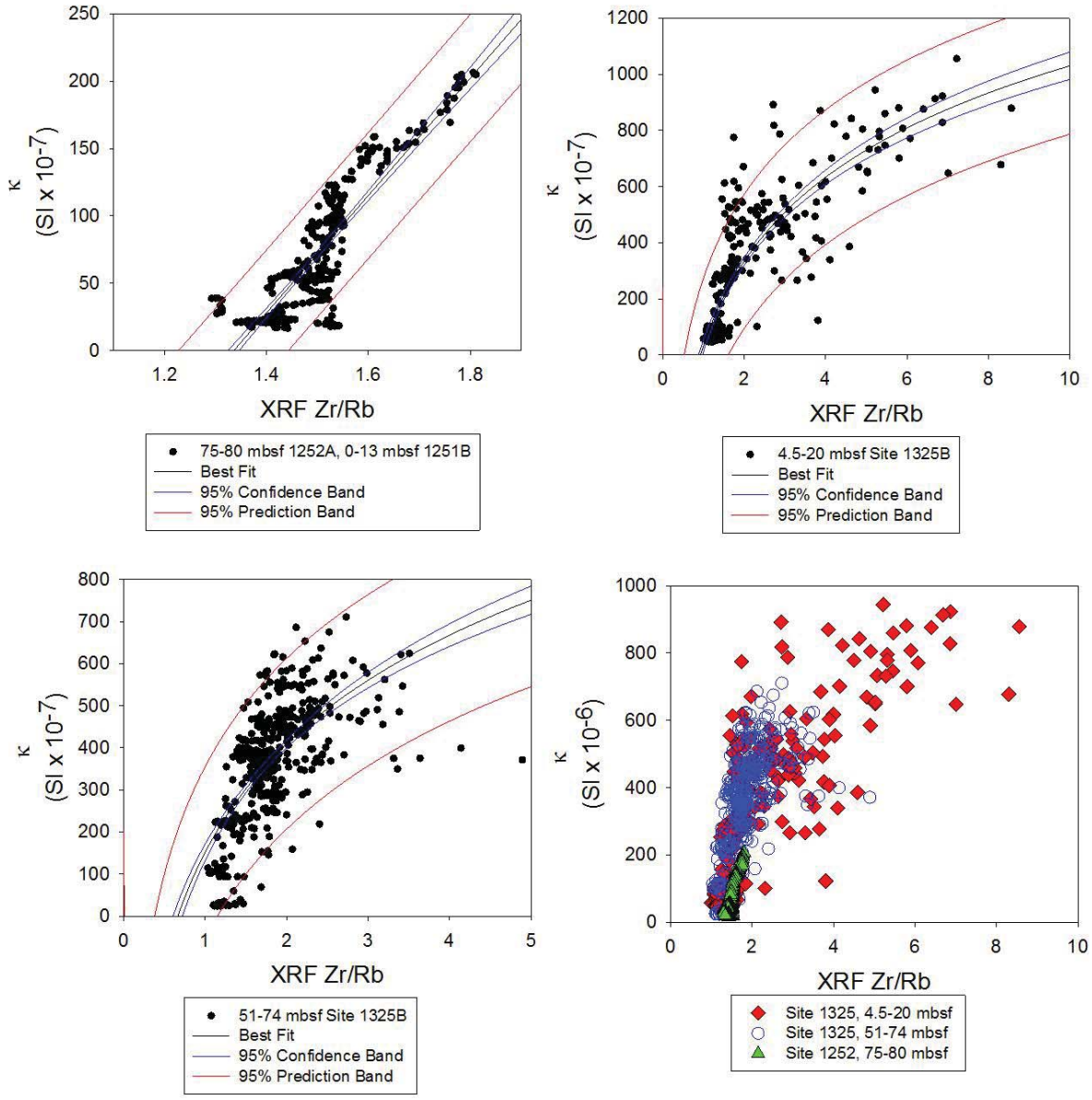

Figure 6. Relationship of XRF Zr/Rb and magnetic susceptibility at Sites 1252A and 1251B (upper left), U1325B 4.5-20 mbsf (upper right), U1325B 51-74 (lower left), all sites (lower right)

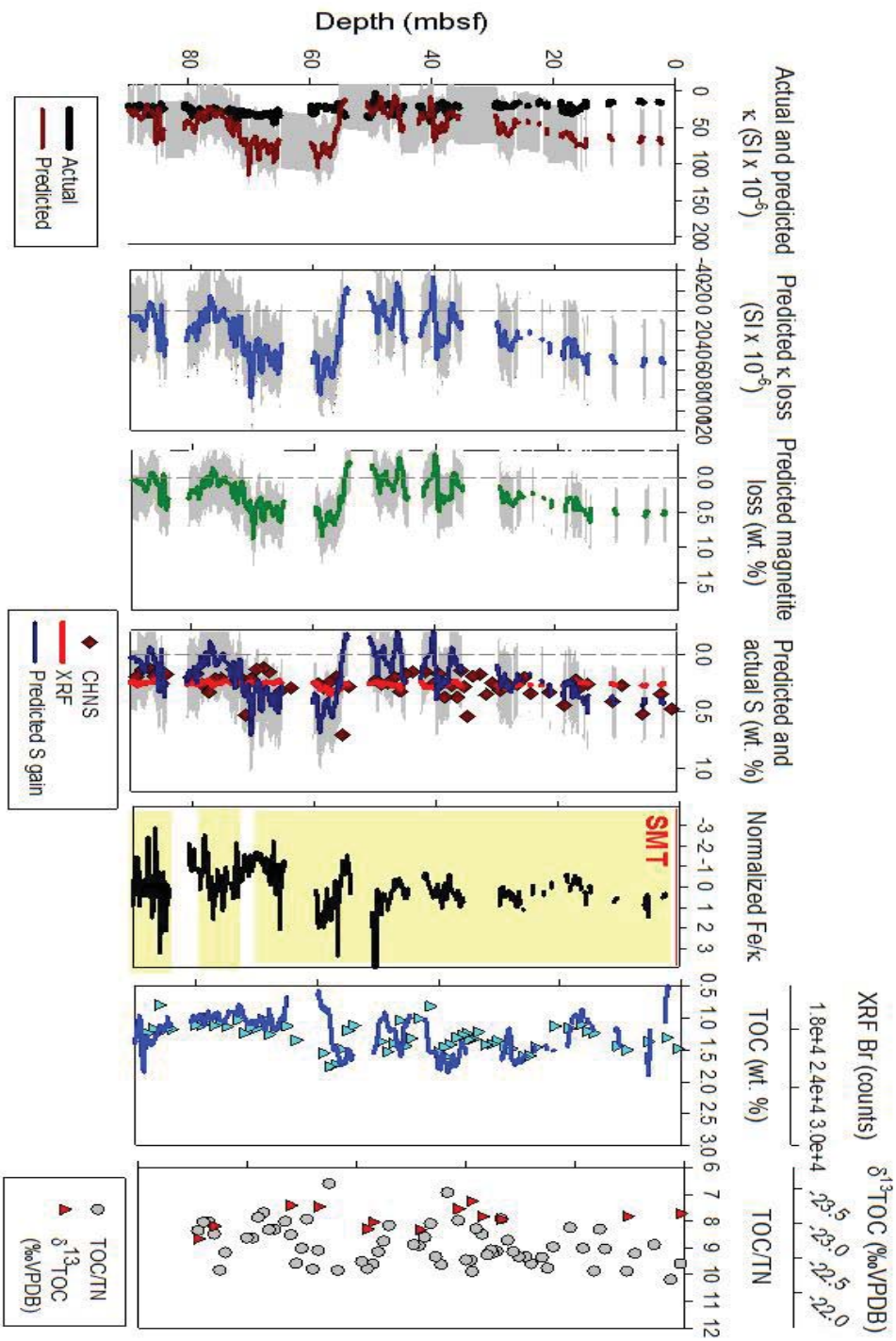

Figure 7. Actual and predicted κ, predicted diagenetic loss of κ, predicted magnetite loss, predicted and actual sulfur precipitation, normalized Fe/κ, TOC with XRF Br, and δ^{13}TOC with TOC/TN at ODP Site 1249.

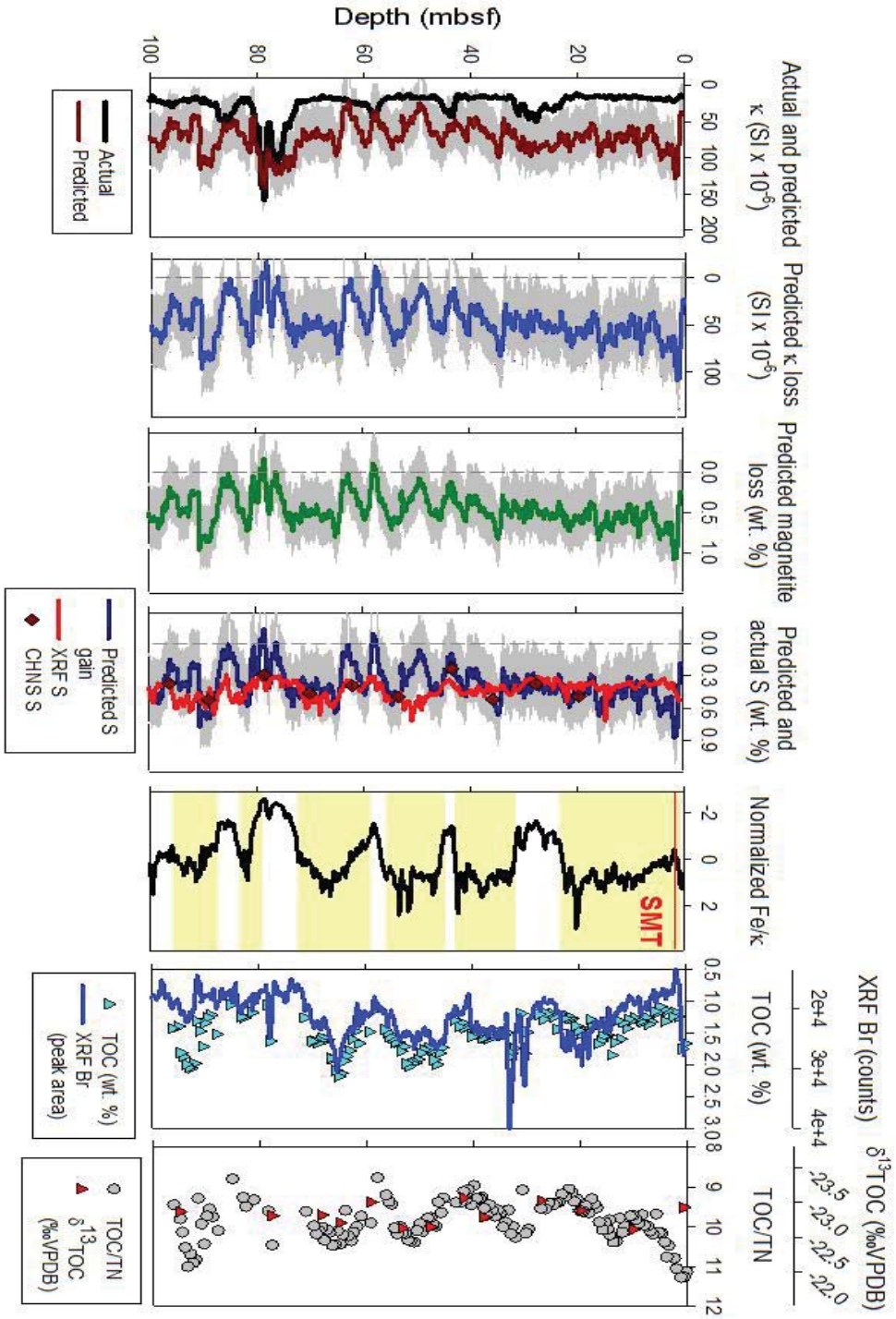

Figure 8. Actual and predicted κ, predicted diagenetic loss of κ, predicted magnetite loss, predicted and actual sulfur precipitation, normalized Fe/κ, TOC with XRF Br, and δ^{13}TOC with TOC/TN at ODP Site 1252.

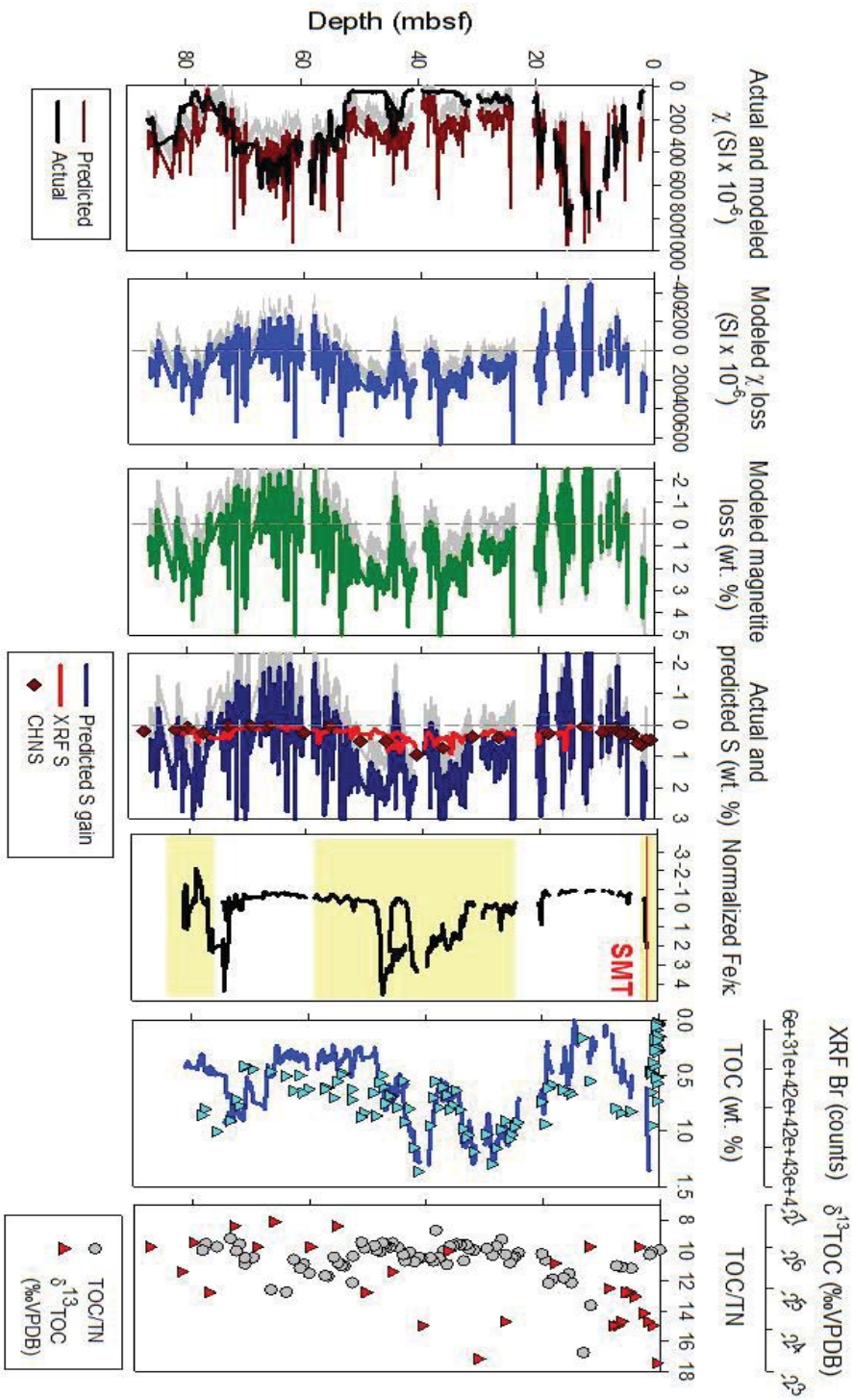

Figure 9. Actual and predicted κ, predicted diagenetic loss of κ, predicted magnetite loss, predicted and actual sulfur precipitation, normalized Fe/κ, TOC with XRF Br, and δ^{13}TOC with TOC/TN at ODP Site U1325.

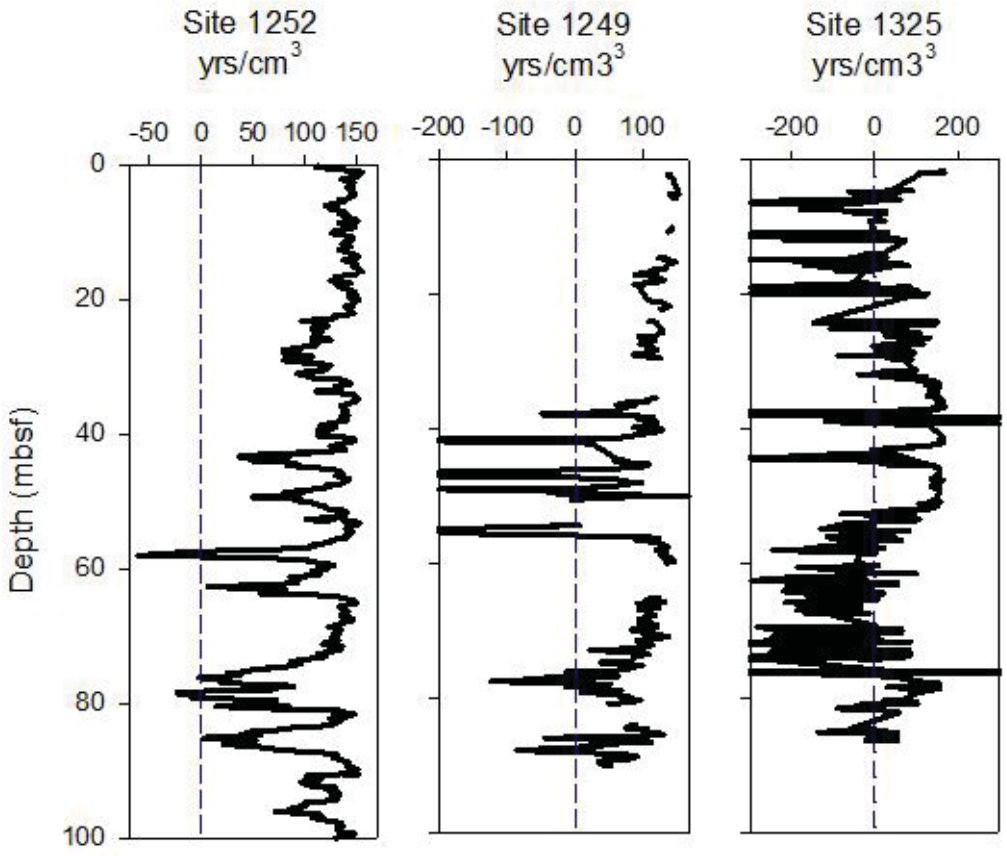

Figure 10. Predicted time in years to account for observed κ loss at ODP Sites 1249 and 1252, and IODP Site U1325.

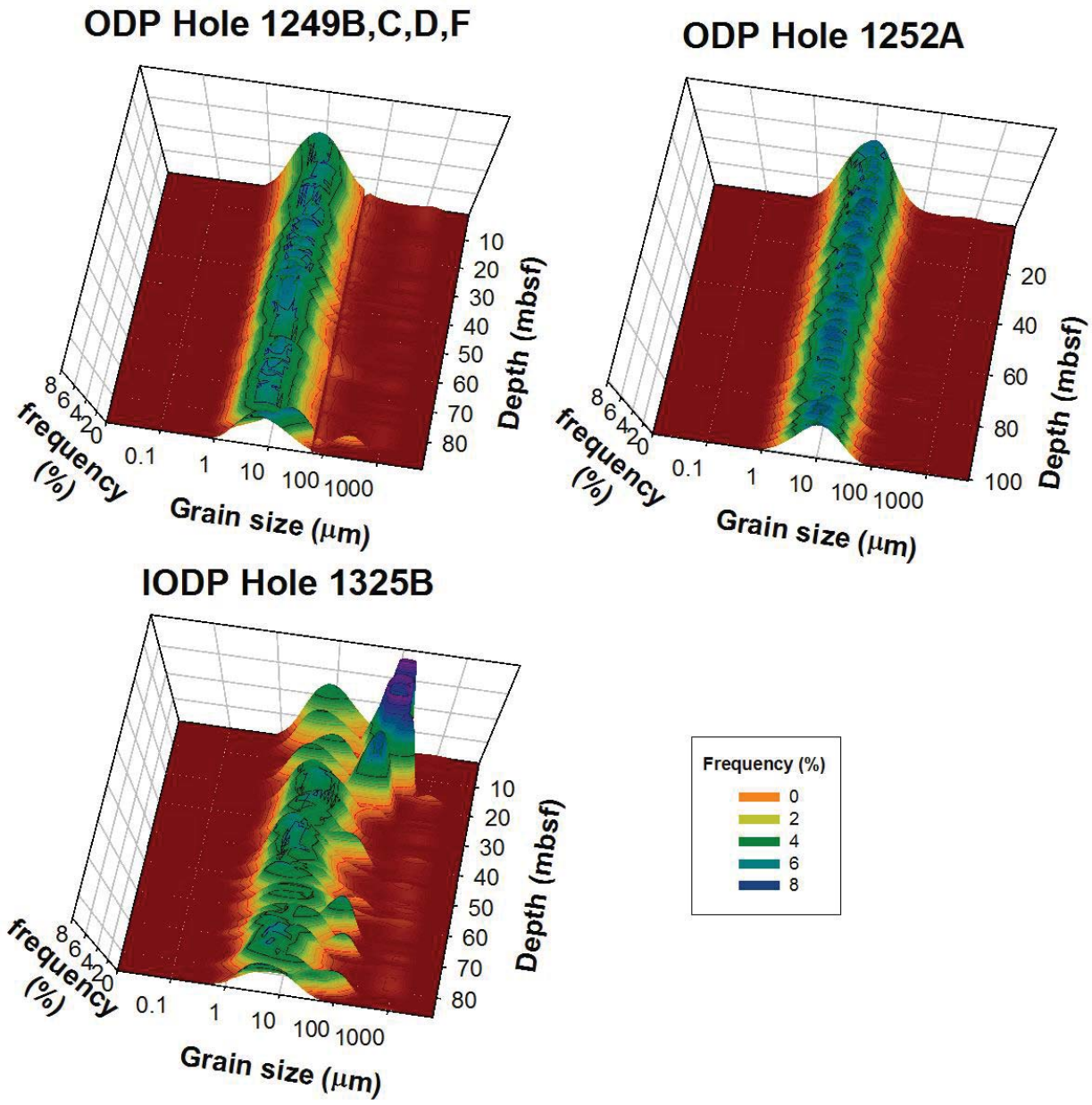

Figure 11. Summary of grain size distribution at ODP Sites 1249 and 1252, and IODP Site U1325.

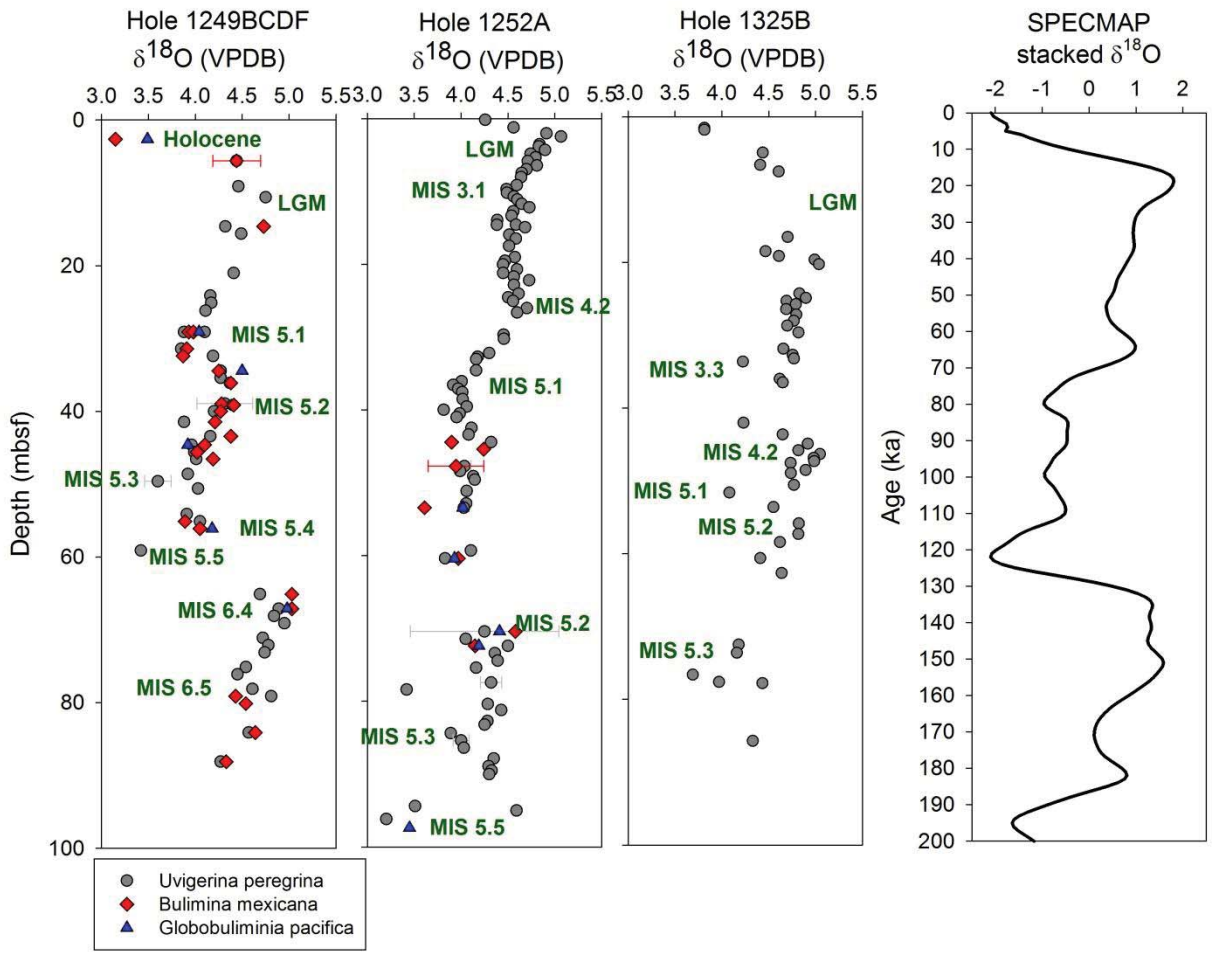

Figure 12. Benthic foraminfer oxygen-isotope record for Sites 1249, 1252, and U1325.

REFERENCES

Berner, R.A., Scott, M.R., and Thomlinson, C., 1970a. Carbonate alkalinity in the pore waters of anoxic marine sediments. Limnology and Oceanography 15, 544-549.

Berner, R.A., 1970b. Sedimentary pyrite formation. American Journal of Science 268, 1-23.

Berner, R.A., 1984. Sedimentary pyrite formation: an update. Geochimica et Cosmochimica Acta, 48:605-615.

Boetius, A., Ravenschlag, K., Schubert C.J., Rickert D., Widdel, F., Gieseke A., Amann R., Jorgensen, B.B., Witte U., Pfannkuche, O., 2000. A marine microbial consortium apparently mediating anaerobic oxidation of methane. Nature 407, 623-626.

Bohrmann, G., Greinert, J., Suess, E., and Torres, M., 1998. Authigenic carbonates from the Cascadia subduction zone and their relation to gas hydrate stability. Geology 26, 647-650.

Borowski, W.S., 2006. Data report: Dissolved sulfide concentration and sulfur isotopic composition of sulfide and sulfate in pore waters, ODP Leg 204, Hydrate Ridge and vicinity, Cascadia Margin, offshore Oregon. In Tréhu, A.M., Bohrmann, G., Torres, M.E., and Colwell, F.S. (Eds.), Proceedings of the Ocean Drilling Program Results 204, 1–13.

Borowski, W.S., Rodriguez, N.M., Paull, C.K., and Ussler III, 2013. Are ^{34}S-enriched authigenic sulfide minerals a proxy for elevated methane flux and gas hydrates in the geologic record? Marine and Petroleum Geology 43, 381-395.

Bloemendal, J., King, J.W., Hall, F.R., and Doh, S.-J., 1992. Rock magnetism of Late Neogene and Pleistocene deep-sea sediments: Relationship to sediment source, diagenetic processes, and sediment lithology. Journal of Geophysical Research 97,4361-4375.

Bloemendal, J., King, J.W., Hunt, A., Demenocal, P.B., and Hayashida, A., 1993. Origin of the sedimentary magnetic record at Ocean Drilling Program sites on the Owen Ridge, Western Arabian Sea. Journal of Geophysical Research 98, 4199-4219.

Blum, P., 1997. Physical properties handbook. ODP Technical Note 26. doi:10.2973/odp.tn.26.1997

Canfield, D.E., and Berner, R.A, 1987. Dissolution and pyritization of magnetite in anoxic marine sediments. Geochimica et Cosmochimica Acta 51, 645-659.

Chamov, N.P., and Murdmaa, I.O., 1995. Coarse fraction minerals of sands in the Cascadia margin sediments. In Carson, B., Westbrook, G.K., Musgrave, R.J., and Suess, E. (Eds.), Proceedings of the Ocean Drilling Program, Scientific Results 146, 33-43.

Childers, A.R., Whitledge, T.E., and Stockwell, D.A., 2005. Seasonal and interannual variability in the distribution of nutrients and chlorophyll a across the Gulf of Alaska shelf: 1998-2000. Deep-Sea Research II 52, 193-216.

Doh, S.-J., King, J.W., and Leinen, M.,1988. A rock-magnetic study of Giant Piston Core LL44-GPC from the Central North Pacific and its paleoceanographic significance. Paleoceanography, 3, 89-111.

Dypvik, H., and Harris, N.B. (2001) Geochemical facies analysis of fine-grained siliciclastics using, Th/U, Zr/Rb, and (Zr+Rb)S/Sr ratios. Chemical Geology 181, 131-146.

Liu, X., and Flemings, P.B., 2006. Passing gas through the hydrate stability zone at southern Hydrate Ridge, offshore Oregon, Earth and Planetary Science Letters, 241. 211-226.

Furukawa, Y., Barnes, H.L., 1995. Reactions forming pyrite from precipitated amorphous ferrous sulfide. In: Vairavamurthy, M.A., Schoonen, M.A.A. (Eds.), Geochemical Transformation of Sedimentary Sulfur. ACS Symposium Series 612, 194–205

Gardner, J.V., Dean, W.E., and Dartnell, P., 1997. Biogenic sedimentation beneath the California Current system for the past 30 kyr and its paleoceanographic significance. Paleoceanography 12, 207-225.

Goldfinger, C., Nelson, C.H., Morey, A.E., Johnson, J.E., Patton, J., Karabanov, E., Gutierrez-Pastor, J., Eriksson, A.T., Gracia, E., Dunhill, G., Enkin, R.J., Dallimore, A., and Vallier, T., 2012, Turbidite event history—Methods and implications for Holocene paleoseismicity of the Cascadia subduction zone: U.S. Geological Survey Professional Paper 1661–F, 170 p, 64 figures, available at http://pubs.usgs.gov/pp/pp1661/f

Greinert, J., Bohrmann, G., Suess, E., 2001. Gas hydrate-associated carbonates and methane-venting at Hydrate Ridge: Classi¢cation, distribution, and origin of authigenic lithologies. In: Paull, C.K., Dillon, W.P. (Eds.), Natural Gas Hydrates: Occurrence, Distribution, and Detection. AGU Geophysical Monograph 124, 99-113.

Hall, F.R., and King, J.W., 1989. Rock-magnetic stratigraphy of Site 645 (Baffin Bay) from ODP Leg 105. In, Srivastava, S.P., Arthur, M., Clement, B., et al., Proceedings of the Ocean Drilling Program, Scientific Results 105, 843-859.

Heeschen, K. U., A. M. Tréhu, R. W. Collier, E. Suess, and G. Rehder, 2003. Distribution and height of methane bubble plumes on the Cascadia margin characterized by acoustic imaging. Geophysical Research Letters 30(12), 1643, doi:10.1029/2003GL016974.

Heeschen, K. U., R. W. Collier, M. A. de Angelis, E. Suess, G. Rehder, P. Linke, and G. P. Klinkhammer, 2005. Methane sources, distributions, and fluxes from cold vent sites at Hydrate Ridge, Cascadia Margin, Global Biogeochemical Cycles 19, GB2016, doi:10.1029/2004GB002266.

Hensen, C., Zabel, M., Pfeifer, K., Schewnk, T., Kasten, S., Riedinger, N., Schulz, H.D., and Boetius, A., 2003. Control of sulfate pore-water profiles by sedimentary events and the significance of anaerobic oxidation of methane for the burial of sulfur in marine sediments. Geochimica et Cosmochimica Acta 67, 2631-2647.

Hepp, D.A., Mörz, T., Hensen, C., Frederichs, T., Kasten, S., Riedinger, N., and Hay, W.F., 2009. A late Miocene-early Pliocene Antarctic deepwater record of repeated iron reduction events. Marine Geology 266, 198-211.

Hinrichs, K.-U., Hayes, J.M., Sylva, S.P., Brewer, P.G., and Delong, E.F., 1999. Methane-consuming archeabacteria in marine sediments. Nature 398, 802-805.

Hoehler, T.M., Alperin, M.J., Albert, D.B., and Martens, C.S., 1994. Field and laboratory studies of methane oxidation in an anoxic marine sediment – evidence for a methanogen-sulfate reducer consortium. Global Biogeochemical Cycles 8, 451-463.

Hunt, C. P., Moskowitz, B. M. and Banerjee, S. K., 1995. Magnetic Properties of Rocks and Minerals. In Ahrens, T.J. (Ed.) Rock Physics & Phase Relations: A Handbook of Physical Constants. American Geophysical Union, Washington, D. C.. doi: 10.1029/RF003p0189

Jicha, B.R., Hart, G.L., Johnson, C.M., Hildreth, W., Beard, B.K., Shirley, S.B., and Valley, J.W., 2009. Isotopic and trace element constraints on the petrogenesis of lavas from Mount Adams volcanic field, Washington. Contributions to Mineralogy and Petrology 157, 189-207.

Johnson, J.E., Goldfinger, C., and Suess, E., 2003. Geophysical constraints on the surface distribution of authigenic carbonates across the Hydrate Ridge region, Cascadia margin. Marine Geology, 202 (1-2) 79-120.

Johnson, J.E., Goldfinger, C., Tréhu, A.M., Bangs, N.L.B., Torres, M.E., and Chevallier. J., 2006, North-South Variability in the History of Deformation and Fluid Venting Across Hydrate Ridge, Cascadia Margin. *In* Tréhu, A.M., Bohrmann, G., Torres, M.E., and Colwell,

F.S. (Eds.), Proc. ODP, *Sci. Results*, 204 [Online]. http://www-odp.tamu.edu/publications/204_SR/125/125.htm

Johnson, J.E., Solway, D., Disenhof, C., Torres, M.E., Hong, W-L., Rose, K., 2010. Identifying slope failure deposits from a potentially mixed magnetic susceptibility signal in gas hydrate bearing regions. Fire in the Ice, National Energy Technology Laboratory Methane Hydrate Newsletter, v. 10, issue 3. http://www.netl.doe.gov/research/oil-and-gas/methane-hydrates/fire-in-the-ice

Johnson, J.E., Phillips, S.C., Torres, M.E., Piñero, E., Rose, K.K., Giosan, L., 2014. Influence of total organic carbon deposition on the inventory of gas hydrate in the Indian continental margins, Marine and Petroleum Geology, 58, 406 424.

Karlin, R., and Levi, S., 1985. Geochemical and sedimentological control of magnetic properties of hemipelagic sediments. Journal of Geophysical Research 90, 10373-10392.

Karlin, R., 1990. Magnetite diagenesis in marine sediments from the Oregon continental margin. Journal of Geophysical Research 95, 4405-4419

Karlin, R.E., and Abella, S.E.B., 1996. A history of Pacific Northwest earthquakes recorded in Holocene sediments from Lake Washington. Journal of Geophysical Research 101, 6137-6150.

Kasten, S., Freudenthal, T., Gingele, F.X., and Shulz, H.D., 1998. Simultaneous formation of iron-rich layers at different redox boundaries in sediments of the Amazon deep-sea fan. Geochimica et Cosmochimica Acta 62, 2253-2264.

Kim, J.-H., and Lee, Y.-J., 2009. Data report: elemental, Rock-Eval, and isotopic compositions of bulk sediments, IODP Expedition 311. In Riedel, M., Collett, T.S., Malone, M.J., and the Expedition 311 Scientists, Proc. IODP, 311:doi:10.2204/iodp.proc.311.207.2009

Kirby, M.E., Domack, E.W., and McClennen, C.E., 1998. Magnetic stratigraphy and sedimentology of Holocene glacial marine deposits in the Palmer Deep, Bellingshausen Sea, Antarctica: implications for climate change? Marine Geology 152, 247-259.

Larrasoaña, J.C., Gràcia, E., Garcés, M., Musgrave, R.J., Piñero, E., Martínez-Ruiz, F., and Vega, M.E., 2006. Rock magnetic identification of magnetic iron sulfides and its bearing on the occurrence of gas hydrates, ODP Leg 204 (Hydrate Ridge). In Tréhu, A.M., Bohrmann, G., Torres, M.E., and Colwell, F.S. (Eds.), Proceedings of the Ocean Drilling Program, Scientific Results, 204: College Station, TX (Ocean Drilling Program), 1–33. doi:10.2973/odp.proc.sr.204.111.2006

Larrasoaña, J.C., Roberts, A.P., Musgrave, R.J., Gràcia, E., Piñero, E., Vega, M., and Martínez-Ruiz, F., 2007. Diagenetic formation of greigite and pyrrhotite in gas hydrate marine sedimentary systems. Earth and Planetary Science Letters, v. 261, p. 350-366.

Liu, Q., Roberts, A.P., Larrasoaña, J.C., Banerjee, S.K., Guyodo, Y., Tauxe, L., and Oldfield, F., 2012. Environmental magnetism: Principles and applications. Reviews of Geophysics 50, RG4002.

Long, P.E., and Wood, B.J., 1986. Structures, textures, and cooling histories of Columbia River basalt flows. Geological Society of America Bulletin, 97, 1114-1155.

Lowrie, W., and Heller, F., 1982. Magnetic properties of marine limestones. Reviews of Geophysics and Space Physics 20, 171-192.

Lynn, R.J., and Simpson, J.J., 1987. The California Current system: the seasonal variability and its physical characteristics. Journal of Geophysical Research 92, 12947-12966.

Milucka, J., Ferdelman, T.G., Polerecky, L., Franzke, D., Wegener, G., Schmid, M., Lieberwirth, I., Wagner, M., Widdel, F., and Kuypers, M.M.M., 2012. Zero-valent sulphur is a key intermediate in marine methane oxidation. Nature doi:10.1038/nature11656ro

Musgrave, R.J., and Hiroki, Y., 2000. Rock magnetism of the diapir sites (Sites 991, 992, 993 and 996), Carolina Rise and Blake Ridge. In Paul, C.K., et al., Proceedings of the Ocean Drilling Program. 164, 401-409.

Neretin, L.N., Böttcher, M.E., Jørgensen, B.B. Volkov, I.I., Lüschen, H., and Higenfeldt, K., 2004. Pyritization processes and greigite formation in the advancing sulfidization front in the Upper Pleistocene sediments of the Black Sea. Geochimica et Cosmochimica Acta 68, 2081-2093.

Nilsson, A., Lee Y.S., Snowball, I., and Hill, M., 2013. Magnetostratigraphic importance of secondary chemical remanent magnetizations carried by greigite (Fe_3S_4) in Miocene sediments, New Jersey shelf (IODP Expedition 313). Geosphere 9, 510-520.

Novosel, I., Spence, G.D., and Hyndman, G.D., 2005. Reduced magnetization produced by increased methane flux at a gas hydrate vent. Marine Geology 216, 265-274.

Peketi, A., Mazumdar, A., Joshi, R.K., Patil, D.J., Srinivas, P.L., and Dayal., A.M., 2012. Tracing the paleo sulfate-methane transition zones and H_2S seepage events in marine sediments: An application of C-S-Mo systematics. Geochemistry Geophysics Geosystems 13, Q10007, doi:10/1029/2012GC004288.

Peterson, T.D., Whitney, F.A., and Harrison, P.J., 2005. Macronutrient dynamics in an anticyclonic mesoscale eddy in the Gulf of Alaska. Deep Sea Research II, 52, 909-932.

Phillips, S.C., Johnson, J.E., Miranda, E., and Disenhof, C., 2011. Improving CHN measurements in carbonate-rich marine sediments. Limnology and Oceanography: Methods 9, 194-203.

Phillips, S.C., Johnson, J.E., Giosan, L., and Rose, K., 2014. Monsoon-influenced variation in productivity and lithogenic sediment flux since 110 ka in the offshore Mahanadi Basin, northern Bay of Bengal. Marine and Petroleum Geology 58A, 502-525, doi:10.1016/j.marpetgeo.2014.05.007.

Prahl, F.G., Ertel, J.R., Goñi, M.A., Sparrow, M.A., and Eversmeyer, B., 1994. Terrestrial organic carbon contributions to sediments on the Washington margin. Geochimica et Cosmochimica Acta 58, 3035-3048.

Pyzik, A.J., and Sommer, S.E., 1981. Sedimentary iron monosulfides: Kinetics and mechanism of formation. Geochimica et Cosmochimica Acta 45, 687-698.

Reeburgh, 1976. Methane consumption in Cariaco Trench waters and sediments. Earth and Planetary Science Letters 47, 345-352.

Reidinger, N., Pfeifer, K., Kasten, S., Garming, J.F.L., Vogt, C., and Hensen, C., 2005. Diagenetic alteration of magnetic signals by anaerobic oxidation of methane related to a change in sedimentation rate. Geochimica et Cosmochimica Acta. 69, 4117-4126.

Rickard, D., Schoonen, M.A.A., and Luther, G.W., 1995. Chemistry of iron sulfides in sedimentary environments. In: Vairavamurthy, M.,A., and Schoonen, M.A.A. (Eds.), Geochemical transformations of sedimentary sulfur. ACS Symposium Series 612, Washington, D.C., p. 168-193.

Rickard, D.,and Luther III, G.W., 1997. Kinetics of pyrite formation by the H_2S oxidation of iron(II) monosulfide in aqueous solutions between 25 and 125 °C: The mechanism. Geochimica et Cosmochimica Acta 61, 135-147.

Robinson, S.G., 1986. The late Pleistocene palaeoclimatic record of North Atlantic deep-sea sediments revealed by mineral-magnetic measurements. Physics of the Earth and Planetary Interiors 42, 22-47.

Sager, W.W., and Hall, S.A., 1990. Magnetic properties of black mud turbidites from ODP Leg 116, distal Bengal Fan, Indian Ocean. In Cochran, J.R., Stow, D.A.V., et al., Proceedings of the Ocean Drilling Program, Scientific Results 116, 317-336.

Schoonen, M.A.A., 2004. Mechanisms of sedimentary pyrite formation. In: Amend, J.P., Edwards, K.J., and Lyons, T.W. (Eds.), Sulfur biogechemistry – past and present. Geological Society of America Special Paper 379, p. 117-134.

Shipboard Scientific Party, 2003. Site 1249. In Tréhu, A.M., Bohrmann, G., Rack, F.R., Torres, M.E., et al. (Eds.) Proceedings of the Ocean Drilling Program, Initial Reports 204, 1-98. doi:10.2973/odp.proc.ir.204.108.2003

Richter T.O., Lassen, S., van Weering, T.C.E., and de Haas, H., 2001. Magnetic susceptibility patterns and provenance of ice-rafted material at Feni Drift, Rockall Trough: implications for the history of the British-Irish ice sheet. Marine Geology 173, 37-54.

Ritger, S., Carson, B., and Suess, E. (1987) Methane-derived authigenic carbonates formed by pore-water expulsion along the Oregon/Washington margin. GSA Bulletin 98, 147-156.

Roberts, A.P., and Turner, G.M., 1993. Diagenetic formation of ferromagnetic iron sulphide minerals in rapidly deposited marine sediments, South Island, New Zealand. Earth and Planetary Science Letters 115, 257-273.

Stoner, J.S, Channell, J.E., and Hillaire-Marcel, C., 1995. Magnetic properties of deep-sea sediments off southwest Greenland: Evidence for major differences between the last two deglaciations. Geology 23, 241-244.

Suess, E., Torres, M.E., Bohrmann, G., Collier, R.W., Greinert, J., Linke, P., Rehder, G., Tre¤hu, A., Wallmann, K., Winckler, G., Zuleger, 1999. Gas hydrate destabilization: Enhanced dewatering, benthic material turnover and large methane plumes at the Cascadia convergent margin. Earth and Planetary Science Letters 170, 1-15.

Suess, E., Torres, M.E., Bohrmann, G., Collier, R.W., Rickert, D., Goldfinger, C., Linke, P., Heuser, A., Sahling, H., Heeschen, K., Jung, C., Nakamura, K., Greinert, J., Pfannkuche, O., Tréhu, A., Klinkhammer, G., Whiticar, M.J., Eisenhauer, A., Teichert, B., and Elvert, M., 2001. Sea floor methane hydrates at Hydrate Ridge, Cascadia margin. In Paull, C.K., and Dillon, W.P. (Eds.), Natural Gas Hydrates: Occurrence, Distribution, and Detection. American Geophysical Union, Geophysical Monogrograph Series 124, 87–98.

Suits, N.S., and Arthur, M.A., 2000. Sulfur diagenesis and partitioning in Holocene Peru shelf and upper slope sediments. Chemical Geology 163, 219-234.

Sweeney, R.E., Kaplan, I.R., 1973. Pyrite framboid formation: laboratory synthesis and marine sediments. Economic Geology 68, 618–634.

Taira, A., and Niitsuma, N., 1986. Turbidite sedimentation in the Nankai Trough as interpreted from magnetic fabric, grain size, and detrital modal analyses. Initial Reports of the Deep Sea Drilling Project 87, 611-632.

Tréhu, A.M., Flemings, P.B, Bangs, N.L., Chevallier, J., Gràcia, E., Johnson, J.E., Liu, X., Riedel, M., and Torres, M.E., 2004. Feeding methane vents and gas hydrate deposits at south Hydrate Ridge, Geophysical Research Letters 31: L23310, doi:10.1029/2004GL021286

Verosub, K.L., and Roberts, A.P., 1995. Environmental magnetism: Past, present, and future. Journal of Geophysical Research 100, 2175-2192.

Wilkin, R.T., and Barnes, H.L., 1996. Pyrite formation by reactions of iron monosulfides with dissolved inorganic and organic sulfur species. Geochimica et Cosmochimica Acta 60, 4167-4179.

LIST OF ACRONYMS AND ABBREVIATIONS

κ	volume-dependent magnetic susceptibility
χ	mass-dependent magnetic susceptibility
AOM	anaerobic oxidation of methane
A_{mag}	surface area of magnetite
$CaCO_3$	calcium carbonate
C_{mag}	magnetite concentration
C_s	hydrogen sulfide concentration
H_2O_2	hydrogen peroxide
HCl	hydrochloric acid
IC	inorganic carbon
IODP	Integrated Ocean Drilling Program
IRM	isothermal remanent magnetism
mbsf	meters below sea floor
ODP	Ocean Drilling Program
PSD	pseudo single domain
SMT	sulfate methane transition
TC	total carbon
TOC	total organic carbon
TN	total nitrogen
VPDB	Vienne Pee Dee Belemnite
wt. %	weight percent

XRF	X-ray fluorescence